Supporting Information

Oxygen vacancy engineering in spinel-structured nanosheets wrapped hollow polyhedrons for electrochemical nitrogen fixation at ambient conditions

Feili Lai,[a,c] Jianrui Feng,[a] Xiaobin Ye,[c] Wei Zong,[a] Guanjie He,[b]* Chao Yang,[d] Yue-E Miao,[a] Bicai Pan,[c] Wensheng Yan,[c] Tianxi Liu,[a]* and Ivan P. Parkin[b]*

[a]State Key Laboratory for Modification of Chemical Fibers and Polymer Materials, College of Materials Science and Engineering, Innovation Center for Textile Science and Technology, Donghua University, Shanghai 201620, P. R. China

[b]Christopher Ingold Laboratory, Department of Chemistry, University College London, 20 Gordon Street, London WC1H 0AJ, U.K

[c]Hefei National Laboratory for Physical Science at the Microscale, University of Science and Technology of China, Hefei, Anhui 230026, P. R. China

[d]Department of Materials Science and Engineering, College of Engineering, Peking University, Beijing 100871, P. R. China

Table of contents

1. Materials synthesis and characterization:

All regents were received from Aladdin Chemical Co., Ltd., and used without any purification.

Synthesis of ZIF-67. In the synthesis of ZIF-67, a methanolic solution (50 mL) of $Co(NO_3)_2•6H_2O$ (249 mg, 1.0 mmol) and 2-methylimidazole (328 mg, 4.0 mmol) were mixed under stirring. Then the mixture was kept reaction at room temperature for 24 h. The bright purple powder of ZIF-67 was collected by centrifugation, washed several times with methanol, and dried at 60 °C.

Synthesis of hollow nitrogen-doped carbon polyhedron (HNCP). Firstly, a homogeneous ZIF-67 dispersion (1 mg mL^{-1}) was prepared, which contains 20 μL of aniline monomer. Subsequently, 30 mL of $(NH_4)_2S_2O_8$ solution (31.7 mg mL^{-1}) was slowly added to the above ZIF-67 dispersion, and was allowed to react overnight. The precipitates were collected by centrifugation, washed several times with deionized water, and dried at 60 °C. Furthermore, 1 M HCl solution was used to remove the ZIF-67 template, after which hollow PANI was obtained after centrifugation, washing and drying. Finally, hollow nitrogen-doped carbon polyhedron was obtained after carbonization at 800 °C for 3 h (ramp rate: 5 °C min^{-1}) under N_2 flow. For comparison, another two nitrogen-doped carbon polyhedrons were synthesized by carbonizing the hollow PANI at 700 and 600 °C for 3 h (ramp rate: 5 °C min^{-1}) under N_2 flow, which were denoted as HNCP(700) and HNCP(600), respectively.

Synthesis of oxygen vacancy-rich $NiCo_2O_4$ at hollow N-carbon polyhedron (V_o-rich $NiCo_2O_4$@HNCP). Typically, 150 mg HNCP powder was dispersed into 30 mL of ethanol/water (*v*:*v* = 1:1) solution containing 110 mg of $Ni(NO_3)_2•6H_2O$, 221 mg of $Co(NO_3)_2•6H_2O$, and 560 mg of methenamine (HMT) under ultrasonication. After reacting at 80 °C for 8 h, the solid product was centrifuged, washed with deionized water/ethanol, and dried at 60 °C, this product was named as nickel-cobalt layered double hydroxide nanosheet wrapped hollow nitrogen-doped carbon polyhedron (Ni-Co LDH@HNCP). Then, the Ni-Co LDH@HNCP powder was heated in air and oxygen atmospheres at 300 °C for 3 h to form oxygen vacancy-rich $NiCo_2O_4$ at hollow N-carbon polyhedron (V_o-rich $NiCo_2O_4$@HNCP) and oxygen vacancy-poor

$NiCo_2O_4$ at hollow N-carbon polyhedron (V_o-poor $NiCo_2O_4$@HNCP), respectively. In addition, another two samples were synthesized by heating Ni-Co LDH@HNCP powder under air condition at 250 and 200 °C for 3 h, which were denoted as V_o-rich $NiCo_2O_4$@HNCP-250 and V_o-rich $NiCo_2O_4$@HNCP-200, respectively.

Replacing HNCP template by HNCP(700) and HNCP(600) templates, another two V_o-rich $NiCo_2O_4$@HNCP(700) and V_o-rich $NiCo_2O_4$@HNCP(600) samples were prepared by using the same step as V_o-rich $NiCo_2O_4$@HNCP.

Synthesis of oxygen vacancy-rich (V_o-rich) Co@HNCP. The V_o-rich and V_o-poor Co@HNCP products were synthesized similarly with the exception of the $Ni(NO_3)_2$•$6H_2O$ precursor.

Synthesis of oxygen vacancy-rich (V_o-rich) ZnCo@HNCP. Typically, 150 mg of HNCP powder was dispersed by ultrasonication into 30 mL solution containing 111 mg of $Zn(NO_3)_2$•$6H_2O$, 221 mg of $Co(NO_3)_2$•$6H_2O$, and certain 30% hydrogen peroxide solution. After mixing all the precursors, the pH of the reactant solution was adjusted to 8 by adding 1 M NaOH solution under a nitrogen atmosphere. After the completion of the reaction, the solid product was centrifuged, washed with deionized water/ethanol, and dried at 60 °C. Then, the above powder was heated in air and oxygen atmospheres at 350 °C to form oxygen vacancy-rich (V_o-rich) ZnCo@HNCP and oxygen vacancy-poor (V_o-poor) ZnCo@HNCP, respectively.

Characterization. Transition electron microscopy (TEM) was carried out on a JEM-2100F electron microscopy. High-resolution TEM (HR-TEM, JEOL ARM 200F) was also operated at an acceleration voltage of 200 kV. X-ray diffraction (XRD) patterns were recorded on a Smartlab X-ray diffractometer (Cu K_α, λ = 0.1542 nm). X-ray photoelectron spectra (XPS) were acquired by an ESCALAB MK II with Mg K_α as the excitation source. The binding energies obtained in the XPS spectral analysis were corrected for specimen charging by referencing C 1s to 284.8 eV. X-ray absorption spectroscopy (XAS) spectra at O *K*-edge, Co *L*-edge and Ni *L*-edge were measured on beamline U19 at National Synchrotron Radiation Laboratory, China. The beam from a bending magnet was monochromatized with a varied line-spacing plane grating monochromator and refocused by a toroidal mirror. N_2 physisorption experiments

were carried out at -196 °C with 40-60 mg sample on a Quadrasorb apparatus from Quantachrome Instruments. Prior to all measurements, the samples were outgassed under vacuum at 150 °C for 20 h. Specific surface areas (SSAs) were calculated using the multi-point Brunauer-Emmett-Teller (BET) model (p/p_0 = 0.05-0.2). Total pore volumes (V_t) were determined at p/p_0 = 0.95. SSAs and V_t were calculated from the data obtained by measurements with 40-60 mg sample. Pore size distributions were calculated using the quenched-solid density functional theory (QSDFT) method (adsorption branch kernel) for N_2 adsorbed on carbon with a slit/cylindrical pore shape at -196 °C. Thermogravimetric analysis (TGA) was conducted with a Netzsch TG 209 F1 device under a constant artificial air flow with a heating rate of 10 °C min^{-1}.

2. Theoretical calculation details:

The Density functional theory (DFT) based computations were implemented by the Vienna *ab initio* simulation package (VASP), with ion-electron interactions depicted by projector augmented waves (PAW) and the exchange and correlation potential described by the function of Perdew, Burke and Ernzerhof (PBE)[1] based on the generalized gradient approximation (GGA). In this calculation, 3 × 3 × 1 and 11 × 11 × 1 Monkhorst-Pack[2] sampled *k* points was used for geometry optimizations and density of states calculations, respectively. Cut-off energy of 400 eV was adopted. The vacuum space is set to be at least 15 Å to separate the interactions between the neighboring slabs. Criteria of convergence was set to 1×10^{-4} eV and 0.01 eV/Å for the self-consistent field (SCF) and ion steps, respectively. The nudged elastic band (NEB) method was used for searching the transition state of the reaction.[3] Spin polarization was considered in all calculations. For depicting the surface of $NiCo_2O_4$, we selected (001) facet for calculating the vacancy formation energy, adsorption energy and the free energy diagram. The vacancy formation energy is referred to O_2 and the NNH adsorption energy is referred to N_2 and H_2. The free energy diagram is plotted at equilibrium potential as $\Delta G = \Delta E + \Delta ZPE - T\Delta S + neU$, where the each item presents free energy, DFT derived energy, zero-point energy, entropy contribution to the free energy and electrode potential contribution to the free energy. Other details follow the previous research.[4]

3. Electrochemical performance measurements:

Cathode preparation. Typically, approximately 1 mg of catalyst and 30 μL of Nafion solution (5 *wt*%) were dispersed in 100 μL of absolute ethanol by sonicating for 1 h to form a homogeneous ink. Then, 30 μL of the homogeneous ink was loaded onto a carbon paper electrode with an area of 1 × 1 cm^{-2} and dried under ambient condition.

Electrochemical NRR measurements. Before NRR tests, Nafion membrane was protonated by first boiling in H_2O_2 5% aqueous solution for 1 h, then in water for another hour, followed by 3 h in 0.5 M H_2SO_4, and finally washed by water several time and kept in water for 6 h. All steps were performed at 80 °C.[5] The Nafion membranes were detected with almost no NH_3 contamination before use. All the electrochemical measurements were carried out on a CHI660B electrochemical workstation (CH Instruments, Inc., Shanghai) with a standard three-electrode system at room temperature (25 °C), by using prepared electrodes, graphite plate and Ag/AgCl electrode as working electrode, counter electrode, and reference electrode, respectively. All the electrochemical measurements were carried out in a sealed container, which will minimize the possibility of contamination from the external environment.[6,7] The potentials reported in this work were converted to reversible hydrogen electrode (RHE) with the following equation:

$$E_{RHE} = E_{Ag/AgCl} + 0.059pH + E^0_{Ag/AgCl} \ (E^0_{Ag/AgCl} = 0.197 \text{ V}) \qquad (1)$$

All inlet pressure of the gas was controlled as 1~3 bar. The open circuit potential experiment of Ar-saturated electrolyte were conducted by purging Ar (≥ 99.999% purity from WUHAN NEWRADAR SPECIAL GAS CO., LTD.) at a flow rate of 20 cm^3 min^{-1} controlled by a mass flow meter (Beijing Sevenstar Flow Co.,Ltd.) for 2 h. For N_2 reduction experiments, the electrolyte of 0.1 M Na_2SO_4 solution was pre-purged with N_2 gas (≥ 99.99% from products description and ≥ 99.999% purity according to pre-delivery inspection for $^{14}N_2$ and ≥ 99.999% from products description for high-purity $^{14}N_2$, WUHAN NEWRADAR SPECIAL GAS CO., LTD.; ≥ 98.5% purity for $^{15}N_2$, Aladdin Chemical Co., LTD.) for 0.5 h before the measurement with different gas flow rate (20 ~ 100 cm^3 min^{-1}), in which a Nafion

membrane separated two-compartment cell with the total volume of 20 mL electrolyte was applied. NRR tests were also conducted under different temperatures (0, 20, 40, and 60 °C) by using circulating water, based on which the temperature-dependent reaction rate can be evaluated by the following Arrhenium equation:

$$v = Ae^{-\frac{E_a}{RT}} \qquad (2)$$

Where v is reaction rate, A is Arrhenius constants, E_a is activation energy, R is gas constant and T is reaction temperature under the absolute scale.

Determination of ammonia. Concentration of produced ammonia was spectrophotometrically determined by the indophenol blue method. First, 2 mL of reaction solution was removed from the electrochemical reaction cell, followed by adding 2 mL of a 1 M NaOH solution containing 5 *wt*% sodium citrate and 5 *wt*% salicylic acid, 1 mL of 0.05 M NaClO, and 0.2 mL of an aqueous solution of 1 *wt*% sodium nitroferricyanide ($C_5FeN_6Na_2O$). After reacting 2 h at room temperature, the corresponding absorption spectrum was measured using ultraviolet-visible spectrophotometer, from which the as-formed indophenol blue can be determined using the absorbance at a wavelength of 660 nm. The concentration-absorbance curve was calibrated using standard NH_4Cl solution with NH_4^+ concentrations of 0.00, 0.16, 0.32, 0.48, 0.64, 0.80, 1.00, and 2.00 μg mL^{-1} in 0.1 M Na_2SO_4 solution. It was shown in Figure S15. The rate of ammonia formation was calculated using the following equation:

$$v_{NH3} = (c_{NH3} \times V)/(t \times A \text{ or } m) \qquad (3)$$

Where v_{NH3} is the rate of ammonia formation, c_{NH3} is the measured NH_3 concentration, V (mL) is the volume of electrolyte, t (h) is the reduction reaction time, and A or m is the geometric area (cm^2) or m (mg) of the catalysts on cathode.

Determination of Faradaic Efficiency (FE). The Faradaic efficiency for NRR was defined as the quantity of electric charge used for synthesizing ammonia divided the total charge passed through the electrodes during the electrolysis. Assuming three electrons were needed to produce on NH_3 molecule, the Faradaic efficiency can be calculated using the following equation:

$$FE = 3F \times c_{NH3} \times V/(17 \times Q) \qquad (4)$$

Where F is the Faradaic constant, Q is the quantity of applied electricity.

$^{15}N_2$ isotope labeling experiments. An isotopic labeling experiment by using $^{15}N_2$ as the feed gas was conducted to clarify the source of ammonia. Before the measurements, the $^{15}N_2$ gas was purified according to the reported Cu trap process.[6] NO_x contamination in both $^{14}N_2$ and purified $^{15}N_2$ gas were also checked *via* purging $^{14}N_2$ and $^{15}N_2$ into electrolyte for 2 h by Nitrite (ULR) Handheld Colorimeter showing 0~6 ppb. After $^{15}N_2$ electroreduction at -0.25 V (*vs.* RHE) in 0.1 M Na_2SO_4 electrolyte for 2 h, the obtained $^{15}NH_4^+$ was quantitatively determined by ^1H nuclear magnetic resonance (NMR, Bruker UlTRASHIELD 400 PLUS). The calibration curves were obtained as follows. Firstly, a series of $^{15}NH_4^+$ solutions with specific concentrations (0, 0.32, 0.64, 1, and 2 μg mL^{-1}) were prepared in 0.1 M Na_2SO_4 solution; secondly, 1 mL of the mixture was identified using ^1H NMR spectroscopy (100 μL of deuterium oxide D_2O was added before NMR detection); thirdly, the calibration was achieved using the peak area ratio of $^{15}NH_4^+$, where the peak area for 2 μg mL^{-1} solution is regarded as a standard. Similarly, the amount of $^{14}NH_4^+$ was quantitatively determined by using this method when $^{14}N_2$ was used as the feed gas.[6-10] Qualitative measurement were conducted by the similar process on NMR (AVANCE3HD 600 MHz).

Determination of hydrazine. The N_2H_4 presented in 0.1 M Na_2SO_4 solution was estimated by the method of Watt and Chrisp.[11] A mixture of *p*-$C_9H_{11}NO$ (5.99 g), HCl (concentrated, 30 mL), and C_2H_5OH (300 mL) was used as a color reagent.

4. Supporting Figures and Tables:

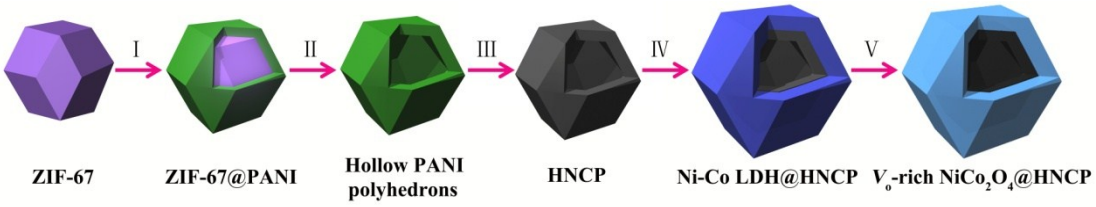

Figure S1. Schematic illustration of the synthesis of the V_o-rich $NiCo_2O_4$@HNCP. (Here, step Ⅰ~V presents *in-situ* polymerization, ZIF removal, carbonization, water bath co-deposition, and annealing, respectively.)

Firstly, rhombic dodecahedral zeolitic imidazolate framework-67 (ZIF-67) was fabricated as a sacrificial template to anchor a uniform polyaniline layer by an *in-situ* polymerization process. After removal of ZIF-67 template by acid etching, a hollow polyaniline polyhedron was generated. Furthermore, hollow nitrogen-doped carbon polyhedron (HNCP) was obtained by a one-step pyrolysis, which is regarded as a strong matrix for solution co-deposition of nickel-cobalt layered double hydroxides (Ni-Co LDH) nanosheets. Finally, V_o-rich $NiCo_2O_4$@HNCP was successfully obtained after an annealing process under air.

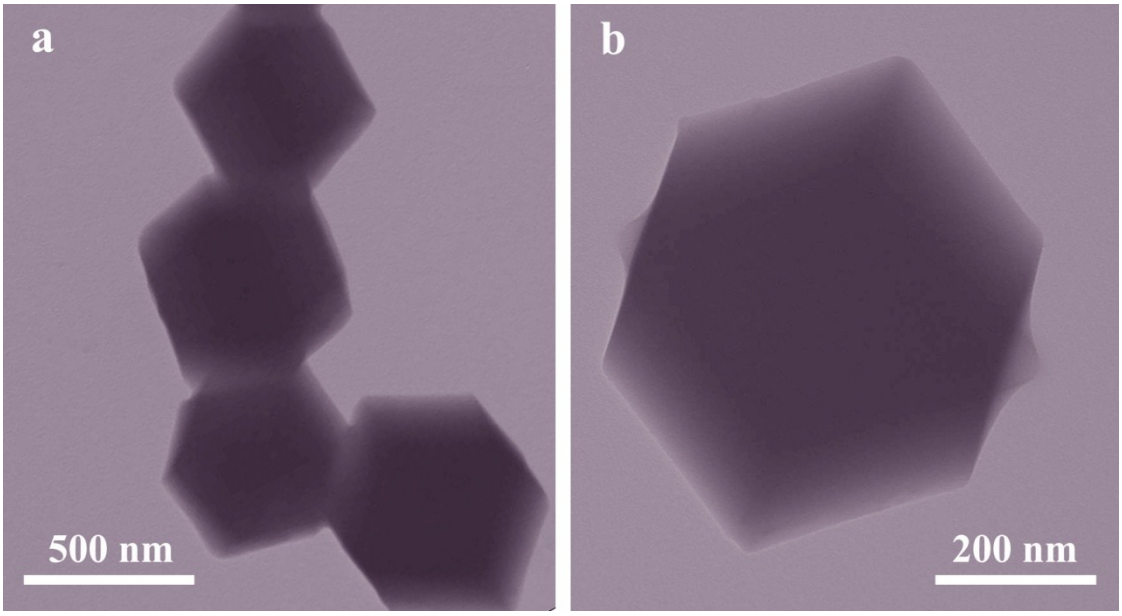

Figure S2. a, b) Transmission electron microscopy (TEM) images of ZIF-67 crystals under different magnifications.

The ZIF-67 crystals of rhombic dodecahedral shape with a diameter of 400 nm were obtained by mixing a methanolic solutions of cobalt nitrate and dimethylimidazole, and keeping the reaction at room temperature (Figure S1).

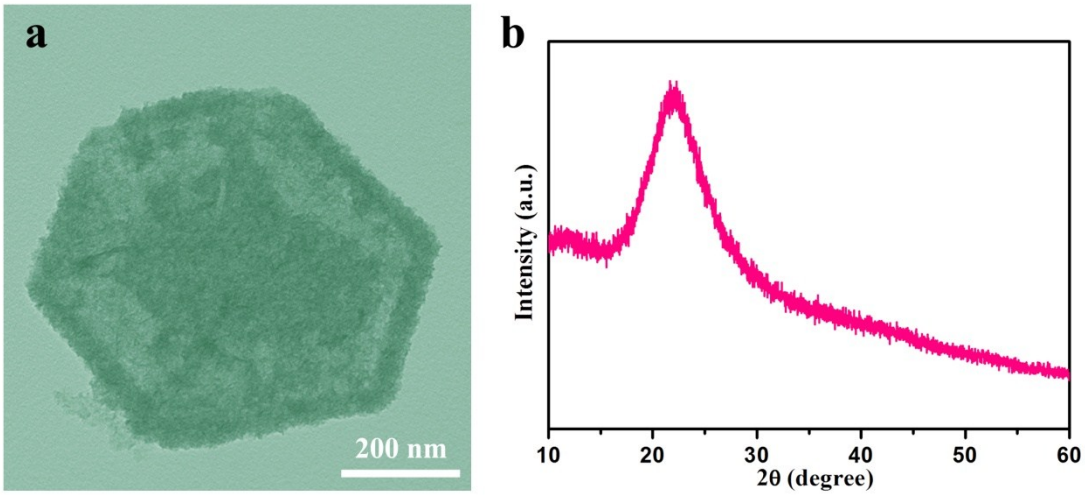

Figure S3. a) TEM image and b) X-ray diffraction (XRD) pattern of HNCP.

The obvious peak at 2θ = 22.4° belongs to a typical (002) interlayer peak of graphite-type carbon (Figure S2), indicating an amorphous structure of the nitrogen-doped carbon template of HNCP.

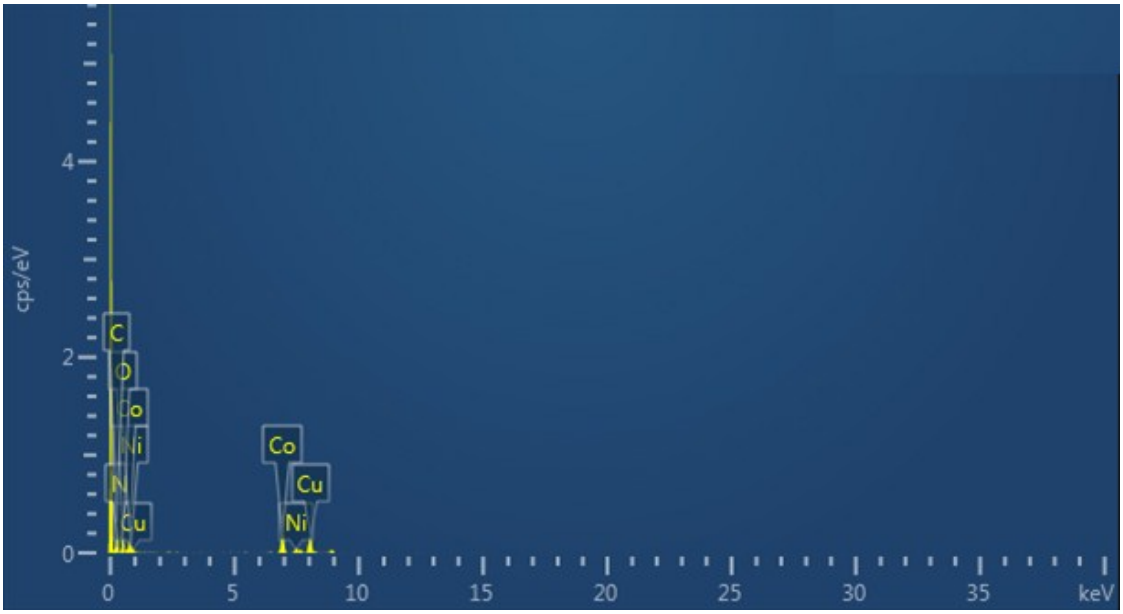

Figure S4. The corresponding energy dispersive spectroscopy (EDS) spectrum of the as-obtained V_o-rich $NiCo_2O_4$@HNCP.

The corresponding energy dispersive spectroscopy (EDS) spectrum in Figure S4 reveals the existence of Ni, Co, C, N, and O elements in the as-obtained V_o-rich $NiCo_2O_4$@HNCP.

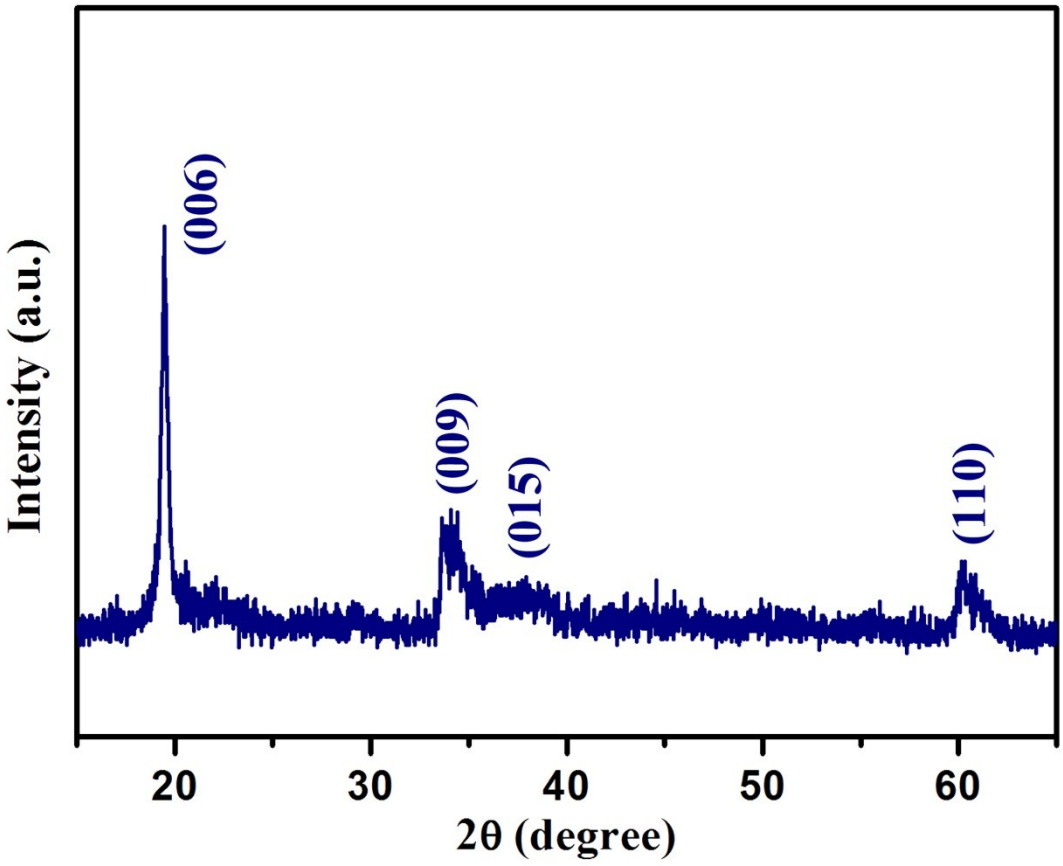

Figure S5. XRD pattern of Ni-Co LDH@HNCP.

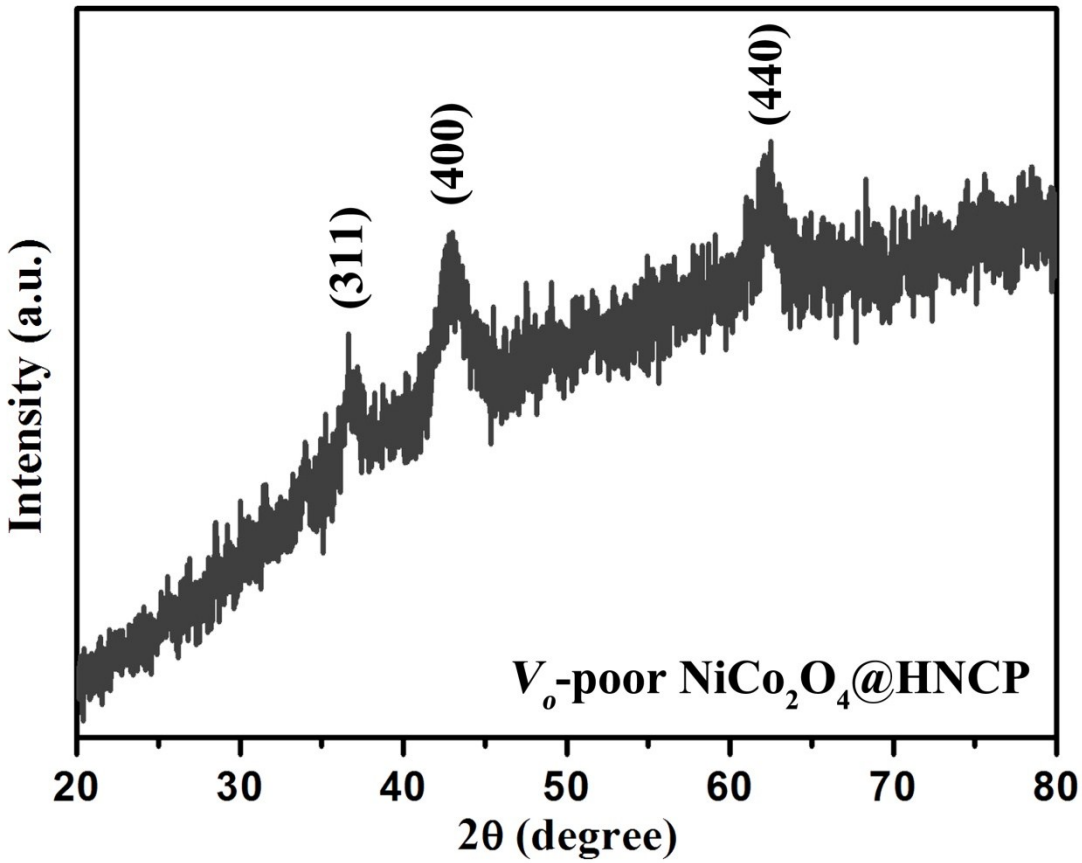

Figure S6. XRD pattern of V_o-poor $NiCo_2O_4$@HNCP.

As shown in Figure S6, the V_o-poor $NiCo_2O_4$@HNCP also shows the typical XRD pattern as V_o-rich $NiCo_2O_4$@HNCP, implying the slightly introduction of oxygen vacancies in $NiCo_2O_4$ did not change its crystal structure.

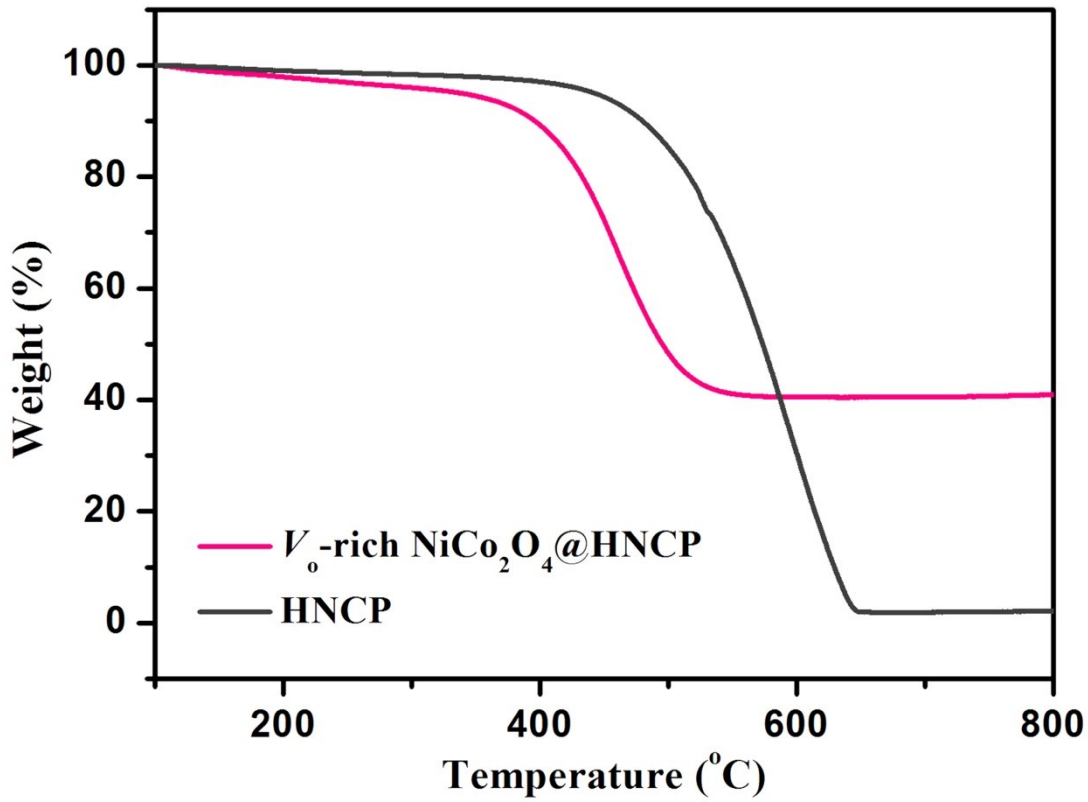

Figure S7. Thermogravimetric analysis (TGA) profiles of V_o-rich $NiCo_2O_4$@HNCP and HNCP.

The weight ratio of V_o-rich $NiCo_2O_4$ nanosheets in V_o-rich $NiCo_2O_4$@HNCP is determined by TGA to be around 40 *wt*% (Figure S7).

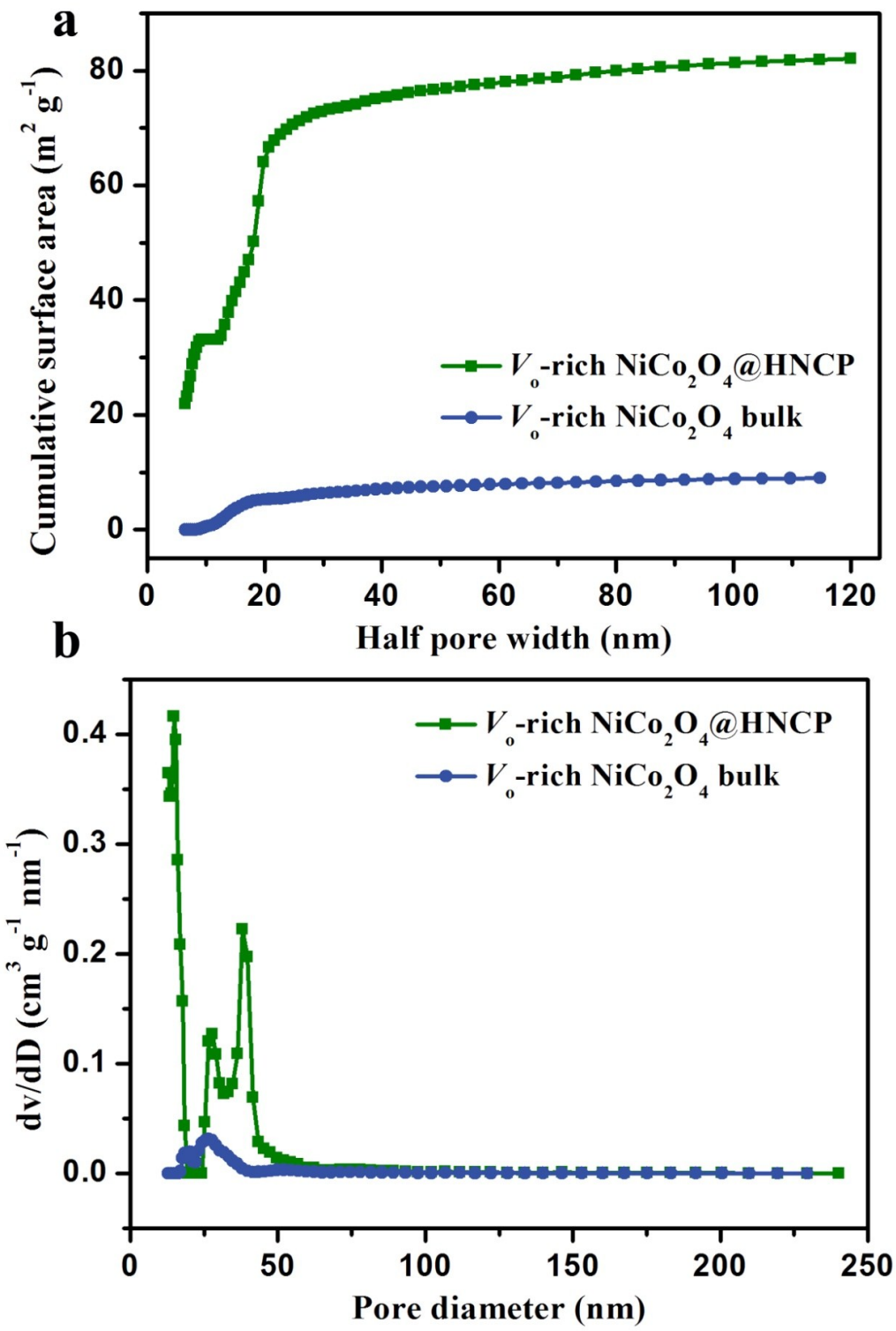

Figure S8. a) Cumulative surface areas and b) pore size distributions of V_o-rich $NiCo_2O_4$@HNCP and V_o-rich $NiCo_2O_4$ bulk.

The V_o-rich $NiCo_2O_4$@HNCP shows a distinct hysteresis loop as a typical type IV isotherm with abundant mesopores located between 25~65 nm (Figure S8).

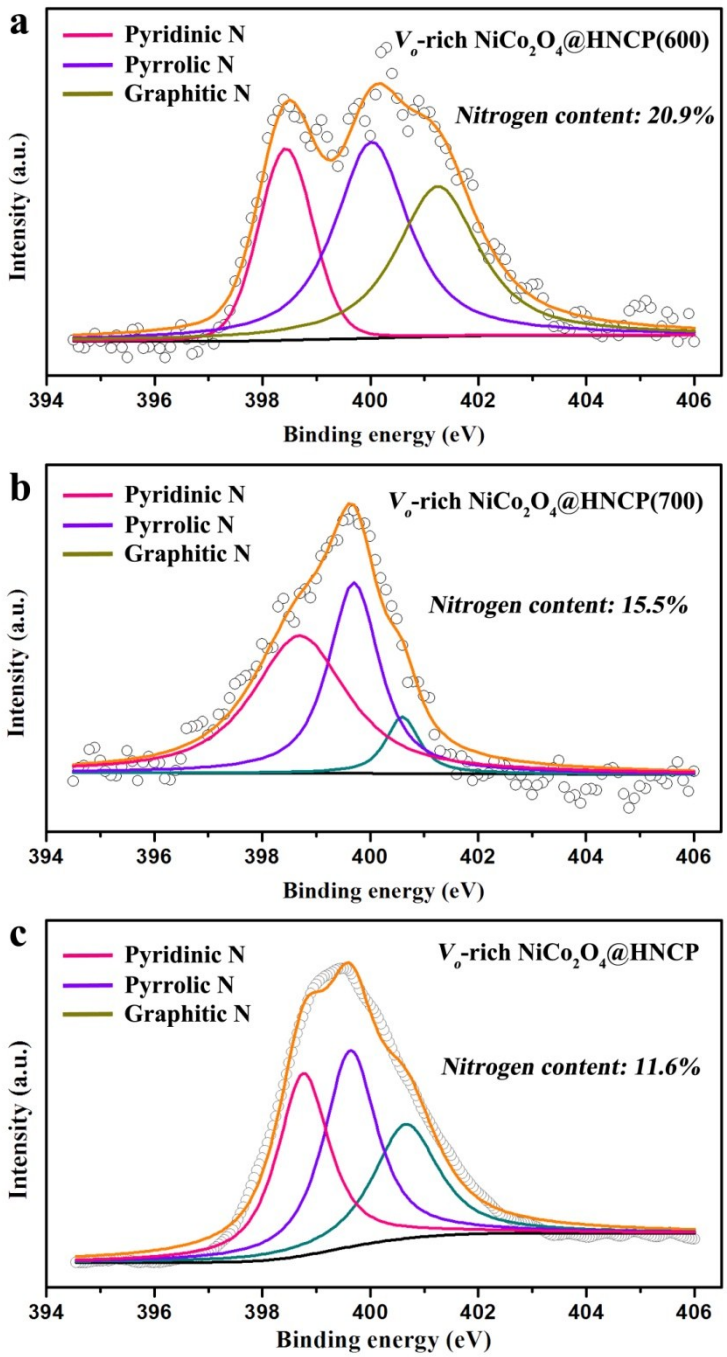

Figure S9. N 1s XPS spectra: a) V_o-rich $NiCo_2O_4$@HNCP(600), b) V_o-rich $NiCo_2O_4$@HNCP(700), and c) V_o-rich $NiCo_2O_4$@HNCP.

As shown in Figure S9, the nitrogen contents in V_o-rich $NiCo_2O_4$@HNCP(600), V_o-rich $NiCo_2O_4$@HNCP(700), and V_o-rich $NiCo_2O_4$@HNCP are calculated to be 20.9, 15.5, and 11.6 *wt*%, demonstrating the decreased nitrogen incorporation as the carbonization temperature increases.

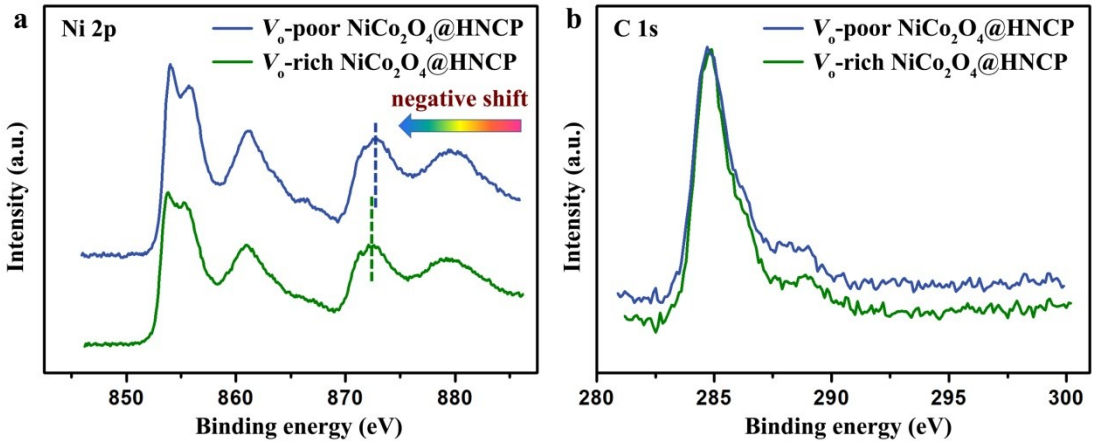

Figure S10. X-ray photoelectron spectroscopy (XPS) spectra for V_o-rich and V_o-poor $NiCo_2O_4$@HNCP: a) Ni 2p, and b) C 1s.

A noticeable peak shift towards low binding energy in Ni 2p XPS spectrum of V_o-rich $NiCo_2O_4$@HNCP is also an evidence of the existence of an oxygen vacancy, indicating the electron transfer from oxygen vacancy to Ni *d* band.

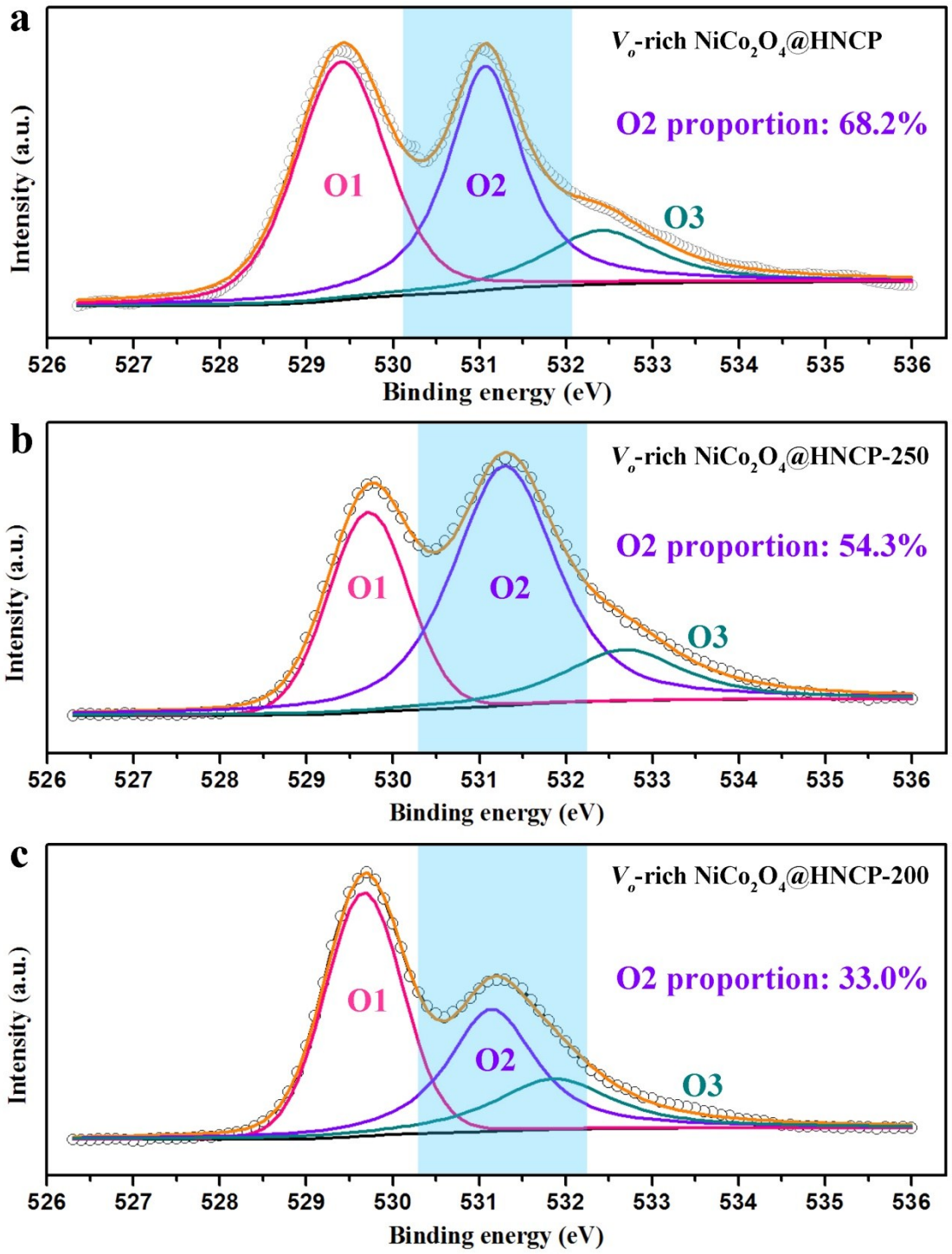

Figure S11. O 1s XPS spectra: a) V_o-rich $NiCo_2O_4$@HNCP, b) V_o-rich $NiCo_2O_4$@HNCP-250, and c) V_o-rich $NiCo_2O_4$@HNCP-200.

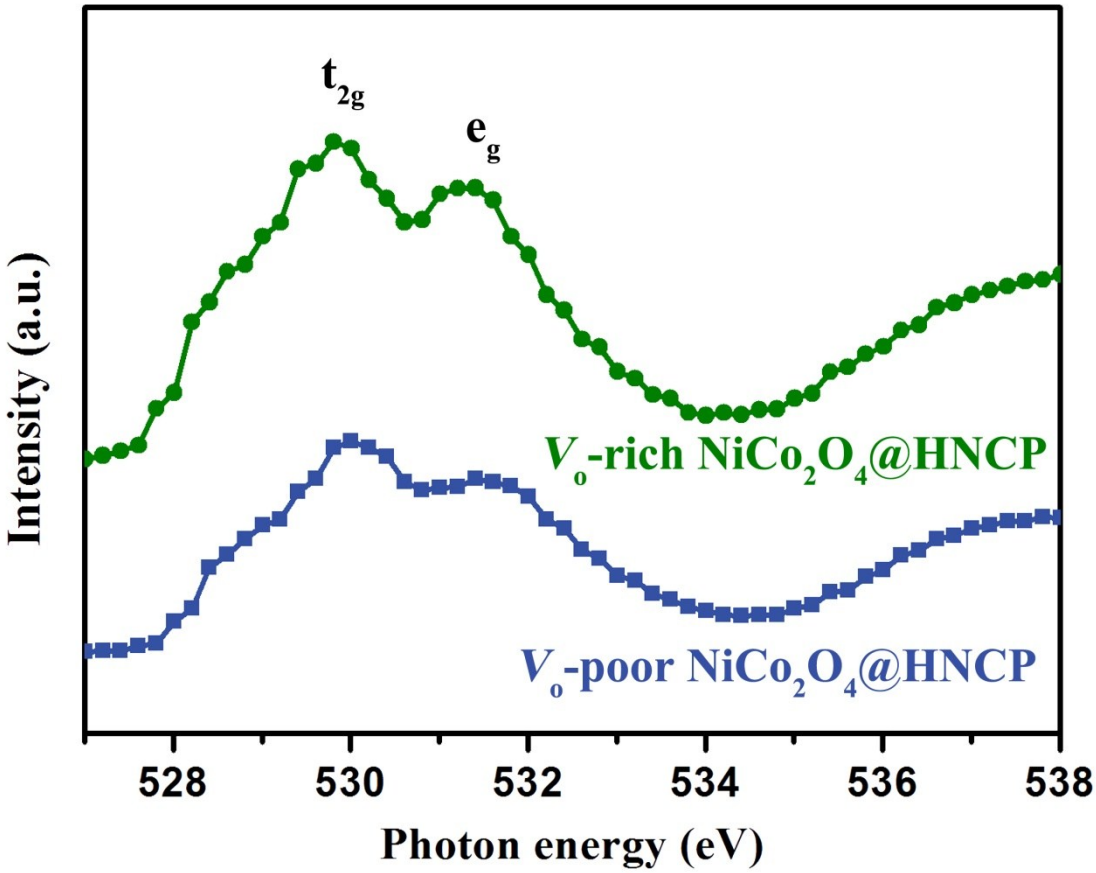

Figure S12. The magnification version of t_{2g} and e_g O *K*-edge for V_o-rich and V_o-poor $NiCo_2O_4$@HNCP.

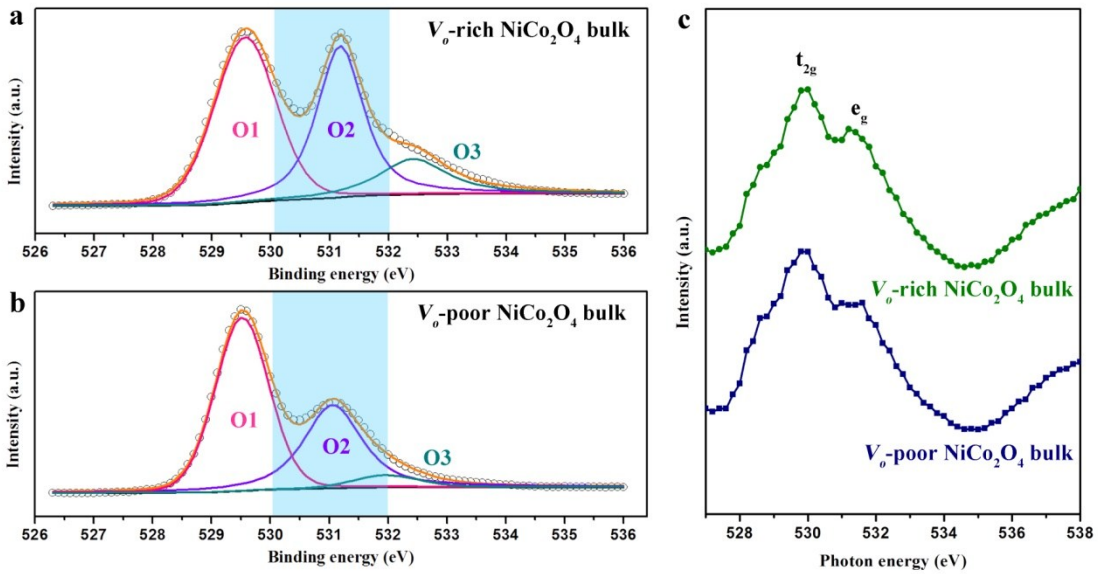

Figure S13. O 1s spectra of a) V_o-rich $NiCo_2O_4$ bulk; and b) V_o-poor $NiCo_2O_4$ bulk; c) The magnification version of t_{2g} and e_g O *K*-edge for V_o-rich and V_o-poor $NiCo_2O_4$ bulks.

Similarly, the results in Figure S13 also give the direct evidence for the generation of oxygen vacancies in the $NiCo_2O_4$ bulk after removing the HNCP template, which demonstrates it is an independent process for the oxygen vacancy incorporation in the $NiCo_2O_4$ crystals.

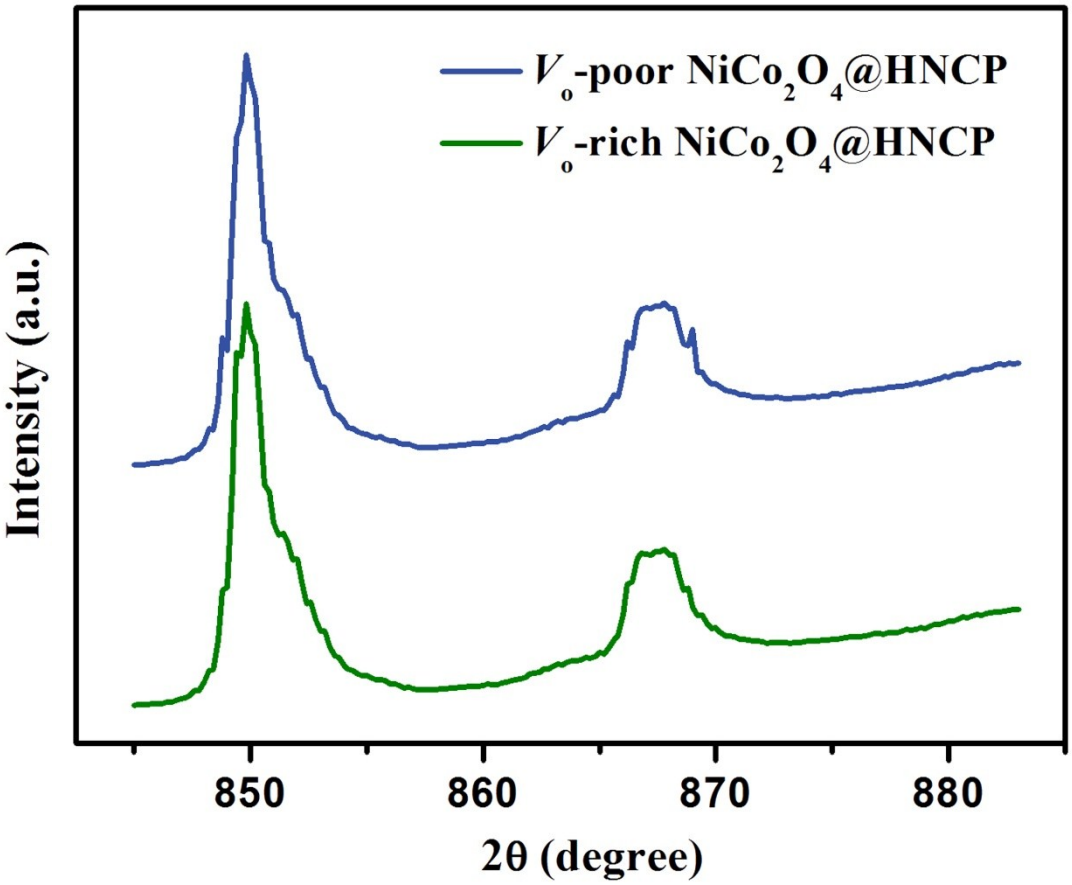

Figure S14. Ni *L*-edge XANES spectra of V_o-rich $NiCo_2O_4$@HNCP and V_o-poor $NiCo_2O_4$@HNCP.

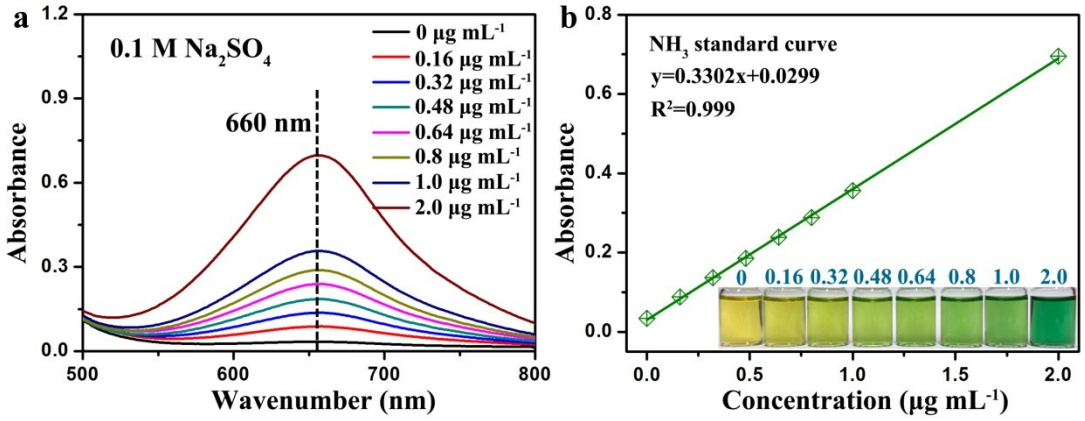

Figure S15. a) UV-Vis curves of indophenol assays with known NH_4^+ concentration after incubated for 2 h; b) Calibration curve used for estimating NH_3 amount by NH_4^+ ion concentration.

The absorbance at 660 nm was measured by UV-Vis spectrophotometer (Figure S15a). The fitting curve (Figure S15b) shows good linear relation of absorbance with NH_4^+ ion concentration ($y = 0.3302x + 0.0299$, $R^2 = 0.999$) of three times independent calibration curves. The inset in Figure S15b shows the indophenol blue solutions with different concentrations of NH_4^+ ions.

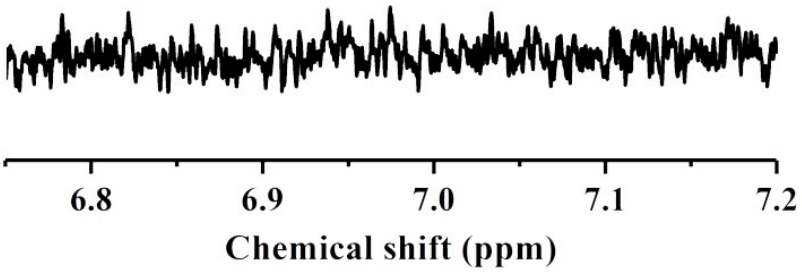

Figure S16. ^{1}H NMR (400 MHz) spectrum of the electrolyte under open circuit potentials with bubbling of Ar gas for 2 h.

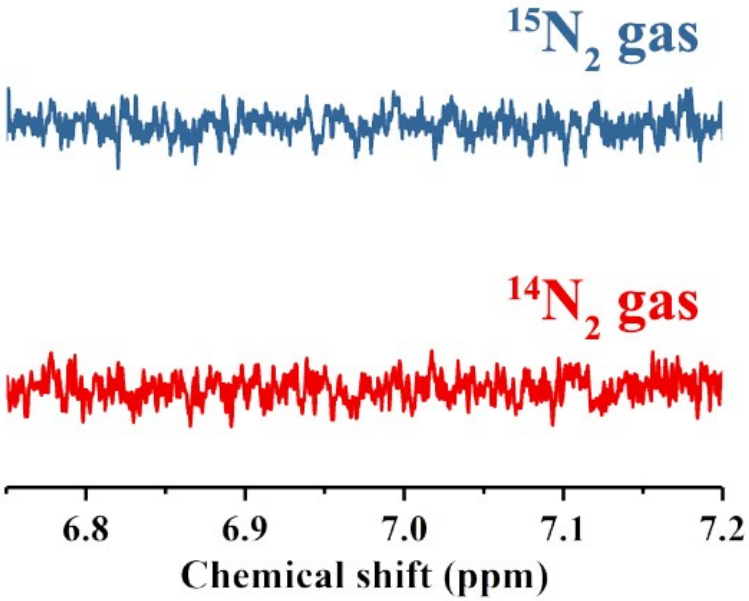

Figure S17. ^{1}H NMR (400 MHz) spectra of the electrolytes under open circuit potentials: a) bubbling purified $^{15}N_2$ for 2 h; b) bubbling $^{14}N_2$ gas for 2 h.

To verify the purity of $^{14}N_2$ and purified $^{15}N_2$ gases, two experiments were conducted under open circuit potentials. As shown in Figure S17, we do not observe obvious signals of ^{14}N triplets and ^{15}N doublets, which demonstrate no obvious contamination affects the detection of produced NH^{4+} in the sealed container.

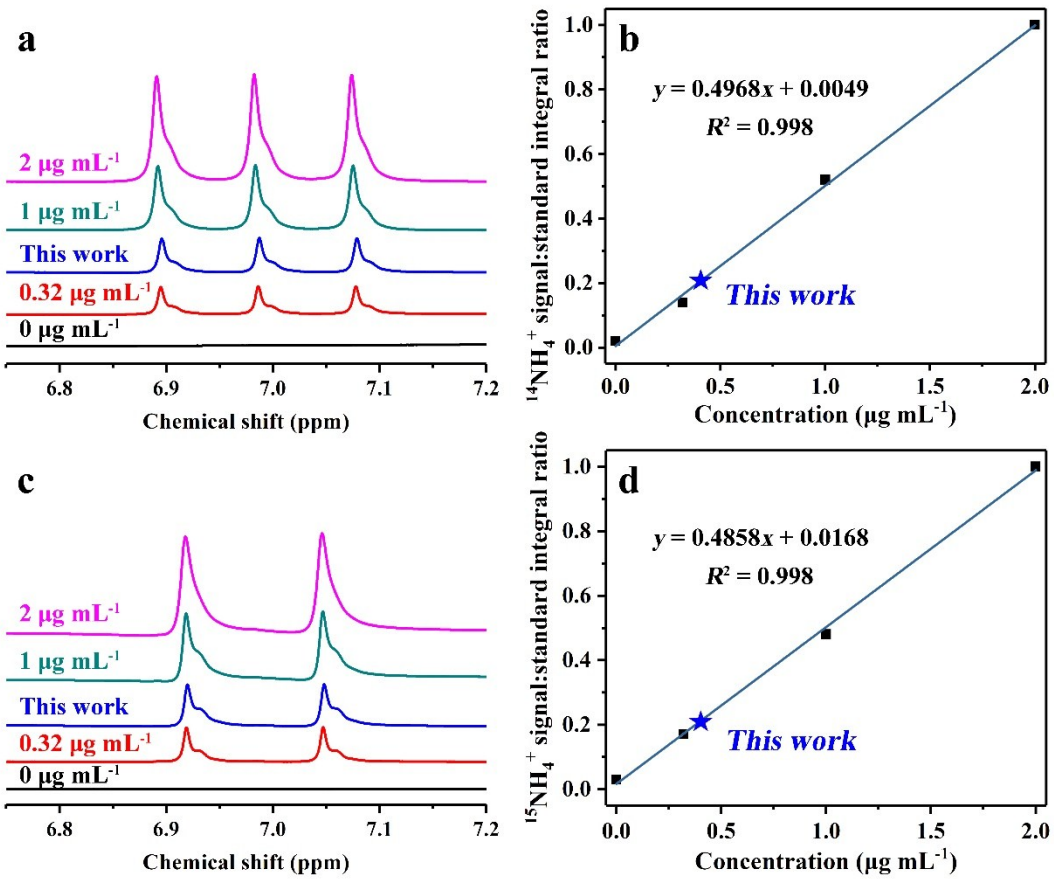

Figure S18. a) ^{1}H NMR spectra (400 MHz) of various $^{14}NH_4^+$ ion concentration and the electrolyte after electrolytic process; b) Integral area ratio against $^{14}NH_4^+$ ion concentration; c) ^{1}H NMR spectra (400 MHz) of various $^{15}NH_4^+$ ion concentration and the electrolyte after electrolytic process; d) Integral area ratio against $^{15}NH_4^+$ ion concentration.

As shown in Figure S18, the similar NH_3 production yields between two analysis methods (NMR and colorimetric method) demonstrate the consistent results in our work. In addition, the similar NH_3 production yields from both $^{14}N_2$ ($^{14}NH_3$: 4.14 μg h^{-1} cm^{-2}) and purified $^{15}N_2$ ($^{15}NH_3$: 4.08 μg h^{-1} cm^{-2}) feed gases also imply the considerable purity of these two gases.

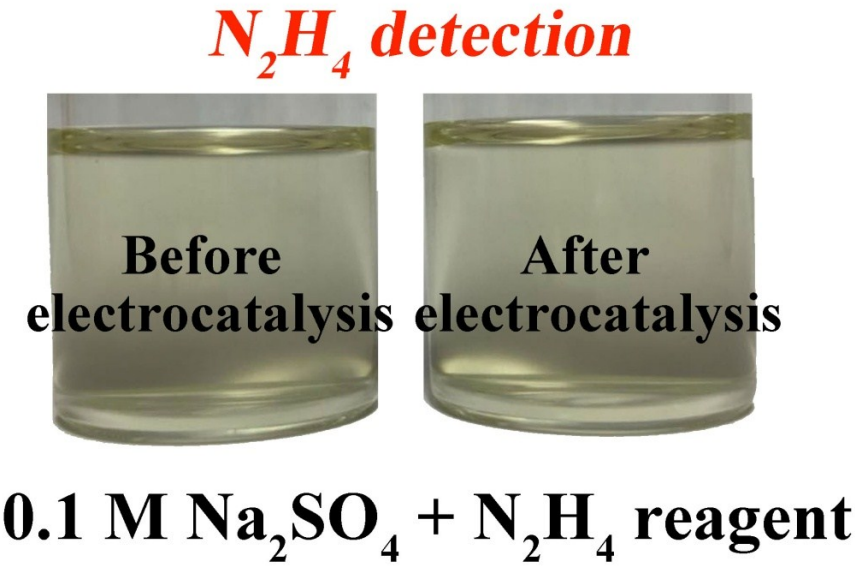

Figure S19. The photographs for mixed solutions of 0.1 M Na_2SO_4 and N_2H_4 reagent before and after electrocatalysis by using V_o-rich $NiCo_2O_4$@HNCP electrocatalyst.

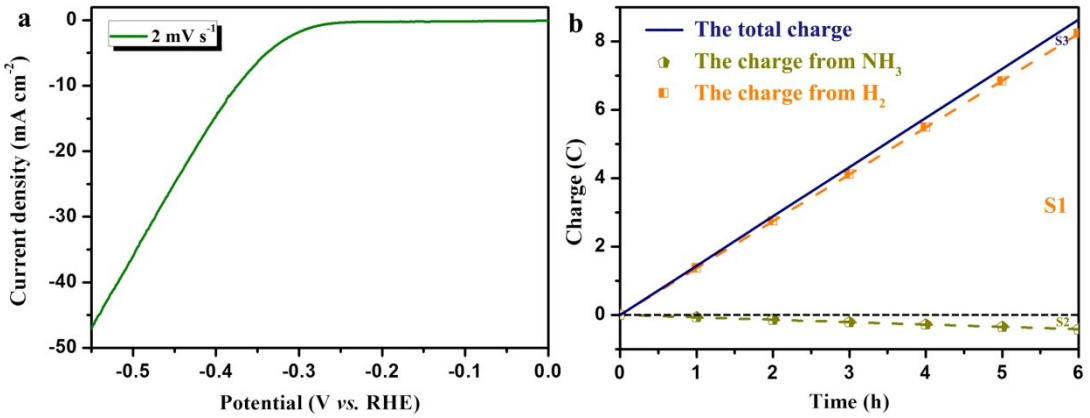

Figure S20. a) Polarization curve of V_o-rich $NiCo_2O_4$@HNCP at a scan rate of 2 mV s^{-1}. b) The amount of theoretically calculated and experimentally measured charges versus time of electrocatalytic NRR and HER processes for V_o-rich $NiCo_2O_4$@HNCP.

As shown in Figure S20, the Faradaic efficiency for hydrogen evolution reaction can be calculated as about 94.5%, leading to a high total Faradaic efficiency of 99.8% towards the sum of hydrogen evolution reaction and nitrogen reduction reaction. The above results indicate that almost all the electrons are only used for the HER and NRR.

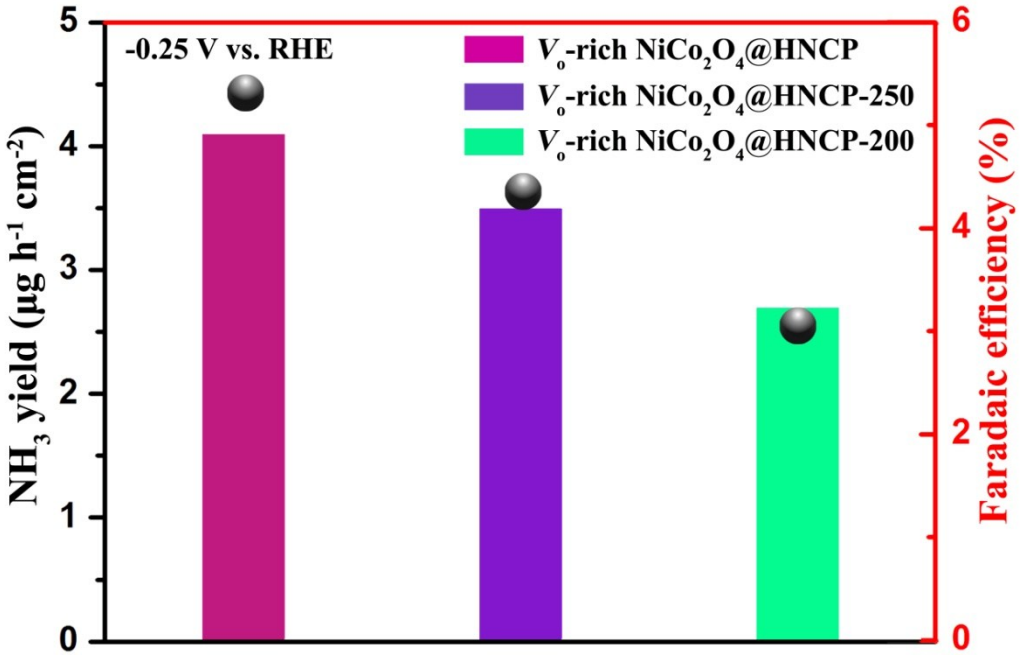

Figure S21. Yield of NH_3 (bar graph) and Faradaic efficiency (black point) after the chrono-amperometry test at -0.25 V versus RHE by using V_o-rich $NiCo_2O_4$@HNCP, V_o-rich $NiCo_2O_4$@HNCP-250, and V_o-rich $NiCo_2O_4$@HNCP-200.

As shown in Figure S21, the average NH_3 yields and corresponding Faradaic efficiencies are decreasing gradually as the annealing temperature decreases from 300 to 200 °C with an interval of 50 °C. By combining the XPS results in Figure S11, it can be concluded that their NRR properties are closely related with the oxygen vacancy concentration in the $NiCo_2O_4$ nanosheets. In detail, the V_o-rich $NiCo_2O_4$@HNCP-200 displays the lowest average NH_3 yield (2.7 μg h^{-1} cm^{-2}) and corresponding Faradaic efficiency (3.1%) at -0.25 V, as compared to those of V_o-rich $NiCo_2O_4$@HNCP-250 (3.5 μg h^{-1} cm^{-2}, 4.3%) and V_o-rich $NiCo_2O_4$@HNCP (4.1 μg h^{-1} cm^{-2}, 5.3%). These results confirm the positive role of oxygen vacancy for enhanced NRR property.

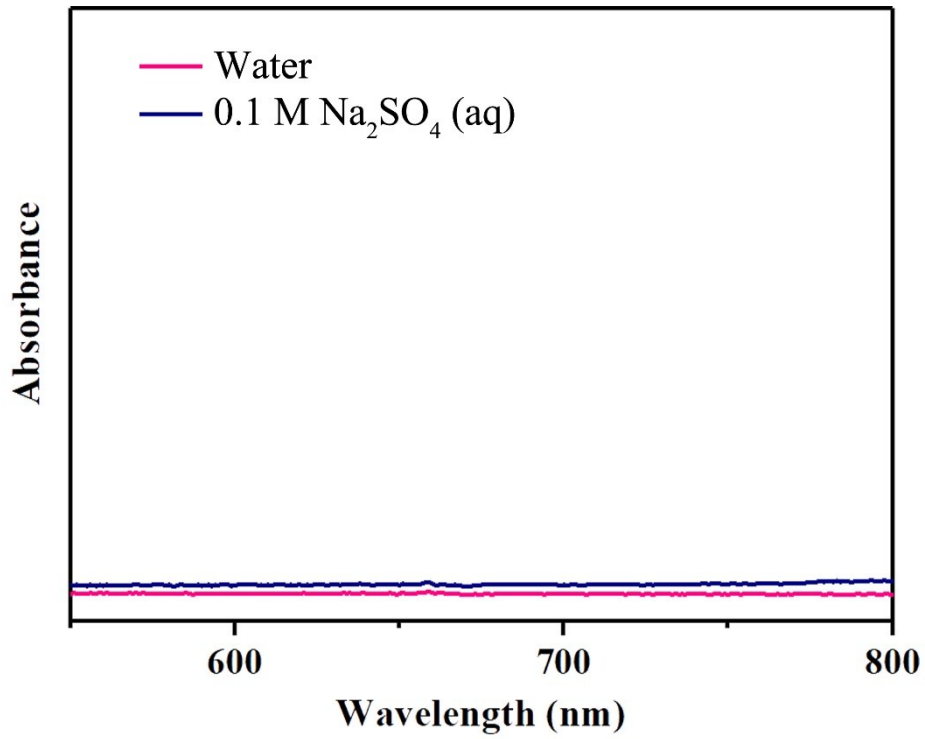

Figure S22. UV-Vis absorption spectra of the 0.1 M Na_2SO_4 and water after incubated for 2 h at room temperature.

As shown in Figure S22, similar UV curves are shown for both water and 0.1 M Na_2SO_4 electrolyte, indicating that Na_2SO_4 would not affect the detection of NH_4^+ concentration.

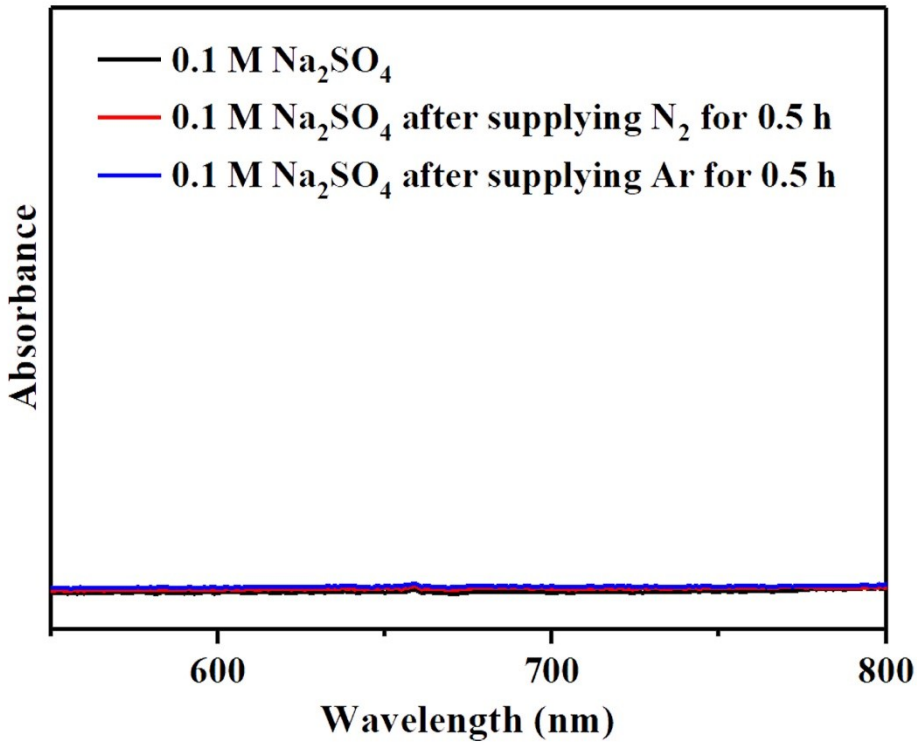

Figure S23. UV-Vis absorption spectra of the 0.1 M Na_2SO_4 electrolyte stained with indophenol indicator before and after continuously supplying N_2 or Ar for 0.5 h at open circuit potentials.

The UV curves in Figure S23 demonstrates that the high purity of N_2 and Ar gases without mixture of NH_3.

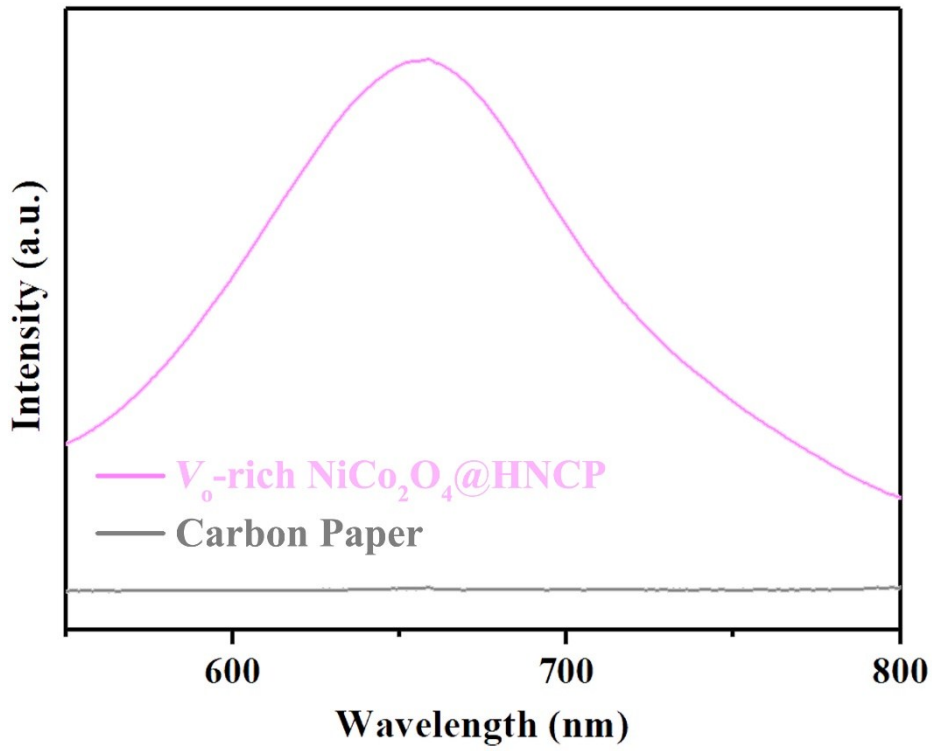

Figure S24. UV-Vis absorption spectra of the electrolyte stained with indophenol indicator after chrono-amperometry test at -0.25 V versus RHE by using V_o-rich $NiCo_2O_4$@HNCP and carbon paper, respectively.

As shown in Figure S24, no NH_3 production can be detected in carbon paper electrode, indicating its negligible effect for N_2 reduction under this potential.

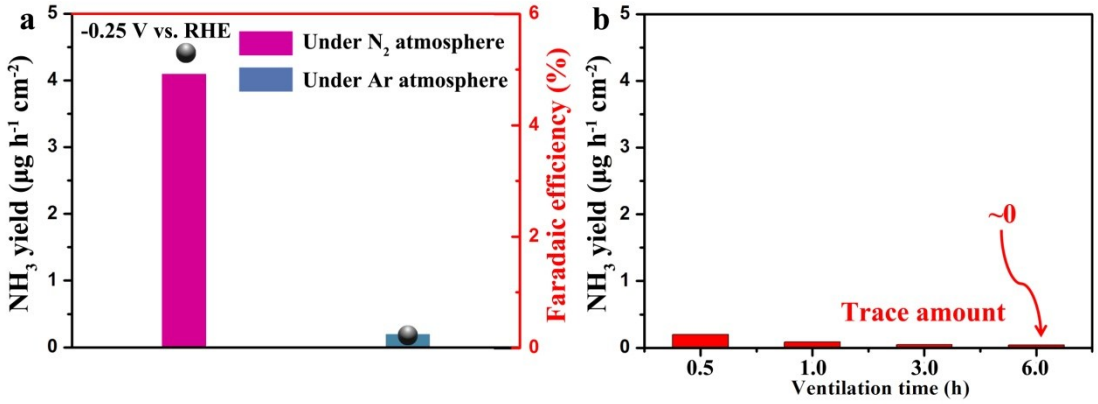

Figure S25. a) Yield of NH_3 (bar graph) and Faradaic efficiency (black point) after chrono-amperometry test at -0.25 V versus RHE by using V_o-rich $NiCo_2O_4$@HNCP under different atmospheres, where the Ar ventilation time is 0.5 h before test. b) Yield of NH_3 by using V_o-rich $NiCo_2O_4$@HNCP under Ar atmosphere with different Ar ventilation time before test.

Here, we found the dissolved N_2 gas in 0.1 M Na_2SO_4 electrolyte can be excluded. There are almost no NH_3 production especially the Ar ventilation time reaches about 6 h (Figure S25).

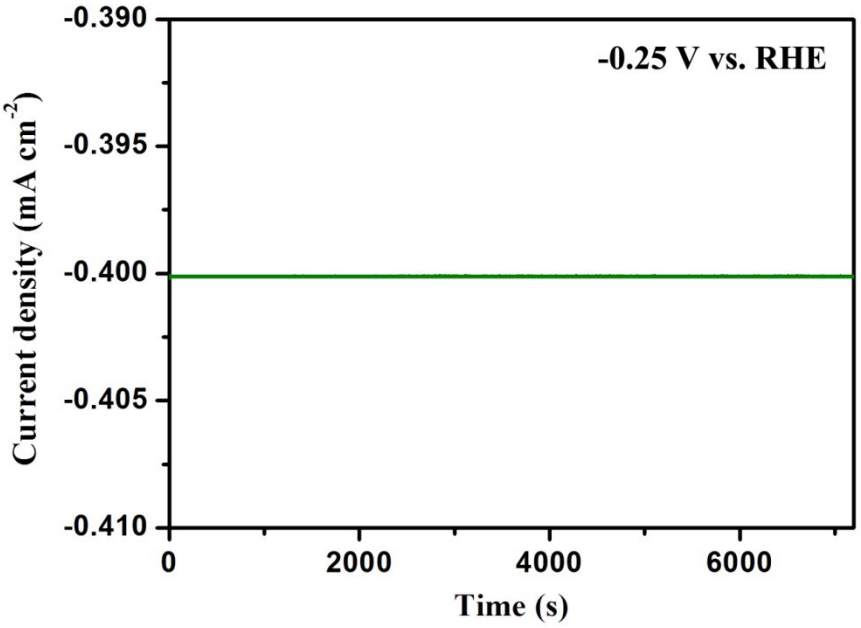

Figure S26. Chrono-amperometry curve at potential of -0.25 V *vs.* RHE by using V_o-rich $NiCo_2O_4$@HNCP catalyst.

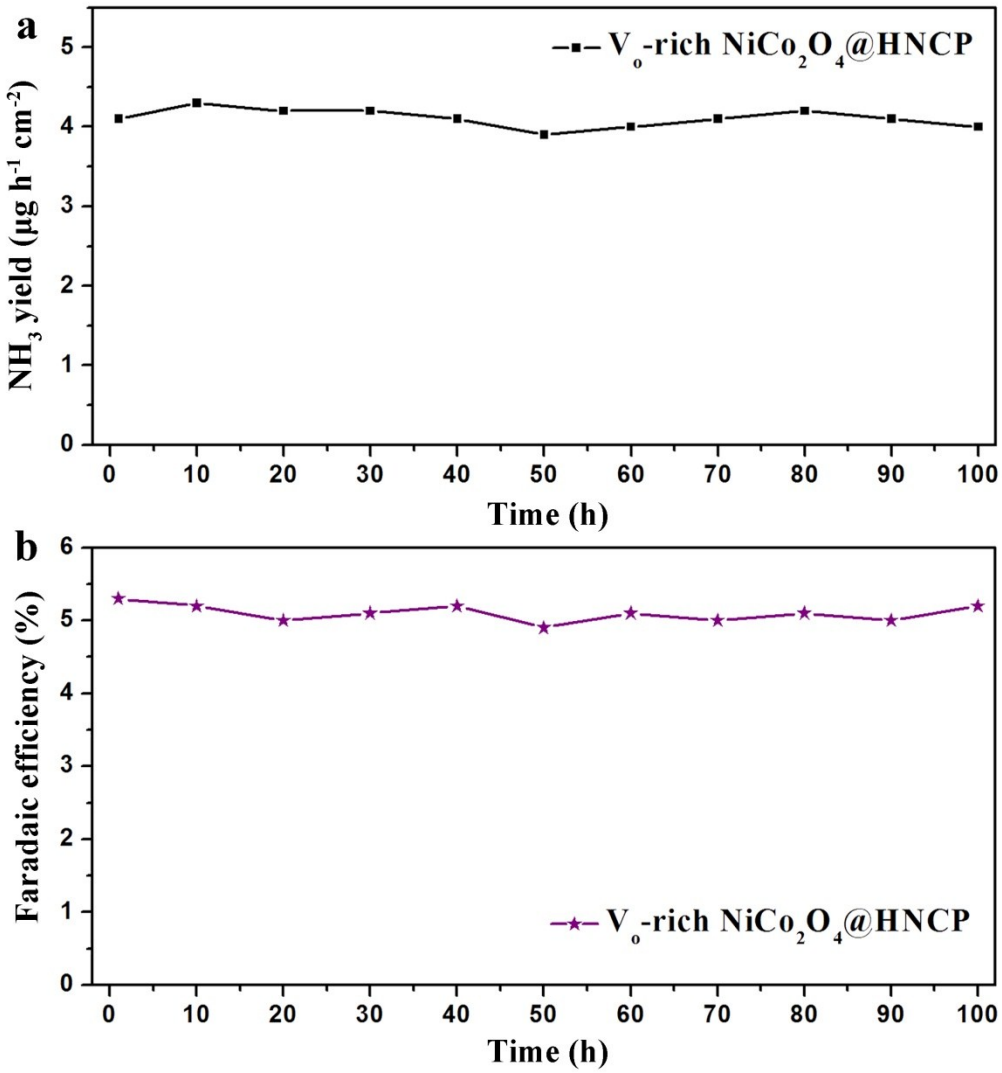

Figure S27. Recycling stability of V_o-rich $NiCo_2O_4$@HNCP catalyst for 100 h at the potential of -0.25 V.

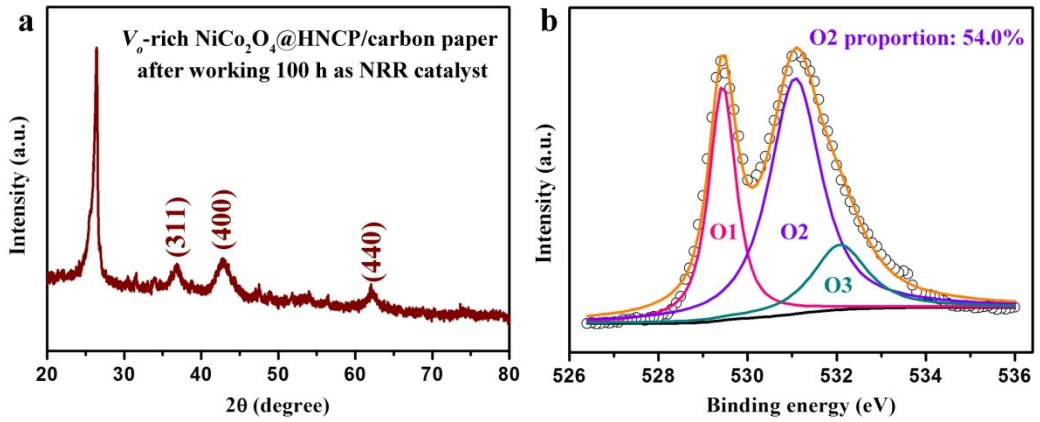

Figure S28. a) XRD pattern, and b) O 1s XPS spectrum of V_o-rich $NiCo_2O_4$@HNCP on carbon paper after working 100 h as NRR catalyst.

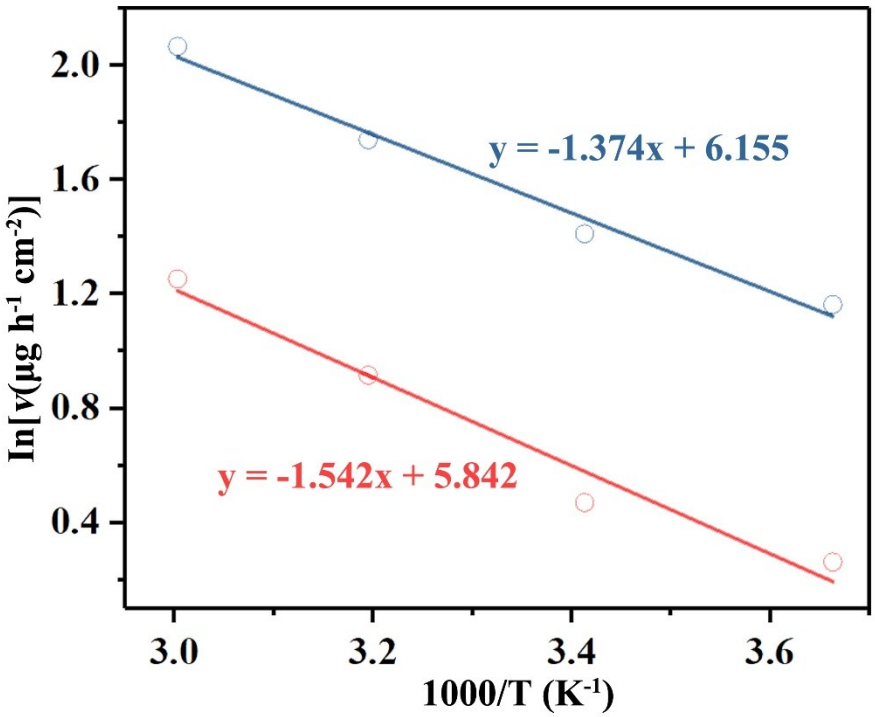

Figure S29. Arrhenius plots of the NRR rates (v) over V_o-rich $NiCo_2O_4$@HNCP and V_o-poor $NiCo_2O_4$@HNCP catalysts at the temperature from 273 to 333 K.

The fitting curves (blue line) show the linear relation of ln(v) with temperature for V_o-rich $NiCo_2O_4$@HNCP (y=-1.374x+6.155) and V_o-poor $NiCo_2O_4$@HNCP (y=-1.542x+5.842). In accordance with the Arrhenius equations and Arrhenius plots (Figure S29), the apparent activation energy for V_o-rich $NiCo_2O_4$@HNCP is calculated to be 11.4 kJ mol^{-1}, which is slightly lower than that of 12.8 kJ mol^{-1} for V_o-poor $NiCo_2O_4$@HNCP, indicating the relatively lower energy barrier by using V_o-rich $NiCo_2O_4$@HNCP as electrocatalyst for nitrogen reduction reactions.

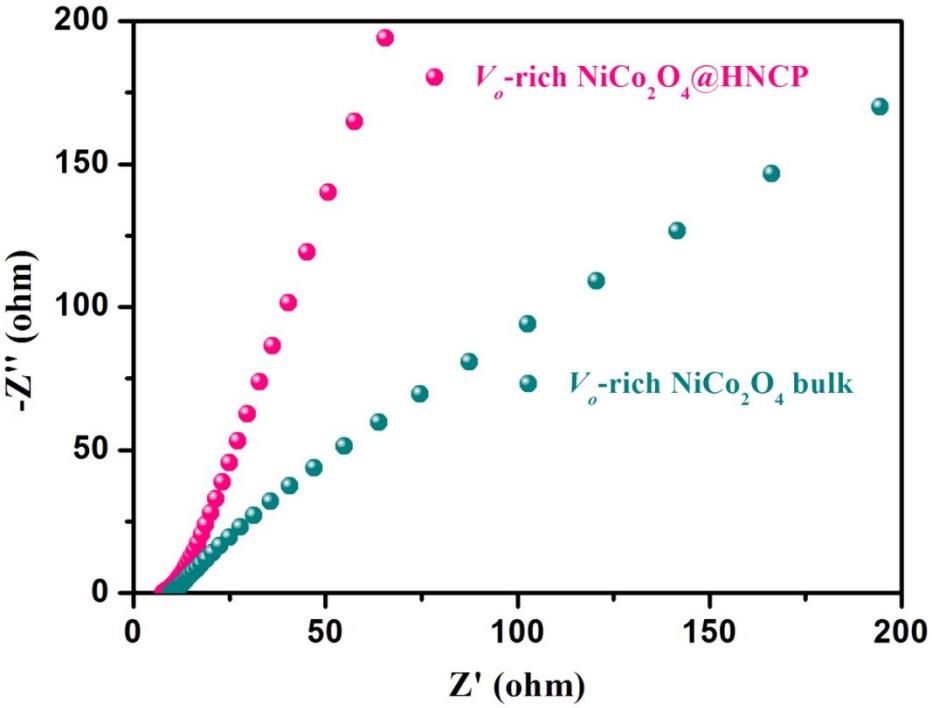

Figure S30. Nyquist plots of V_o-rich $NiCo_2O_4$@HNCP and V_o-rich $NiCo_2O_4$ bulk.

As shown in Figure S30, the vertical slope of the linear part in the low frequency region indicates the quicker electron transfer and lower diffusion resistance of ions in V_o-rich $NiCo_2O_4$@HNCP as compared with that of V_o-rich $NiCo_2O_4$ bulk.

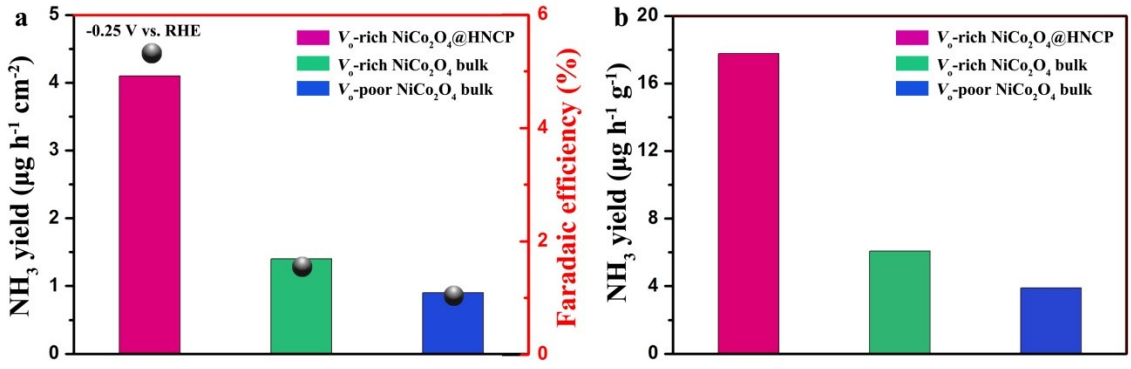

Figure S31. Yield of NH_3 (bar graph) and Faradaic efficiency (black point) after chrono-amperometry test at -0.25 V versus RHE by using V_o-rich $NiCo_2O_4$@HNCP, V_o-rich $NiCo_2O_4$ bulk, V_o-rich $NiCo_2O_4$ bulk catalysts.

After comparing with the V_o-rich $NiCo_2O_4$ bulk (1.4 μg h^{-1} cm^{-2}/6.1 μg h^{-1} mg^{-1}, 1.6% at -0.25 V) in Figure S31, it was proved that the hollow nitrogen-doped carbon polyhedron template in V_o-rich $NiCo_2O_4$@HNCP is extremely vital for its enhanced NRR performance, due to the increased specific surface area (Figure 2d), and well-formed interface between HNCP and V_o-rich $NiCo_2O_4$ nanosheets for charge accumulation/transfer. Meanwhile, the V_o-rich $NiCo_2O_4$ bulk also possesses an enhanced NRR performance as compared with that of V_o-poor $NiCo_2O_4$ bulk, which provides the direct evidence for the positive role of oxygen vacancy in V_o-rich $NiCo_2O_4$ nanosheets.

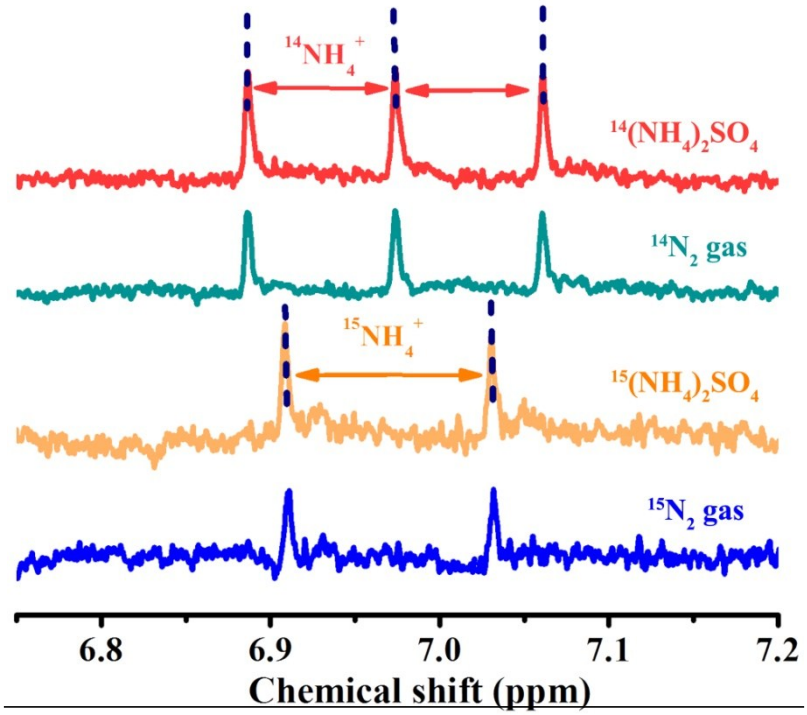

Figure S32. ^{1}H NMR spectra (600 MHz) of $^{15}NH_4^+$ and $^{14}NH_4^+$ produced from the NRR reaction using $^{15}N_2$ and $^{14}N_2$ as the feeding gas.

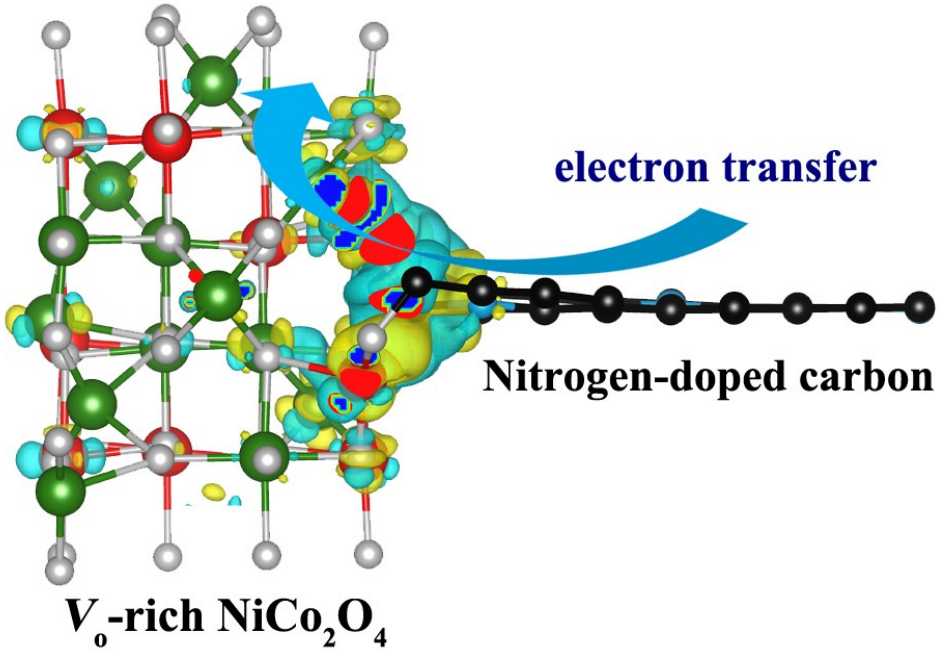

Figure S33. Charge density distribution of V_o-rich $NiCo_2O_4$@HNCP around the interface and oxygen vacancy with efficient electron transfer from nitrogen-doped carbon to V_o-rich $NiCo_2O_4$.

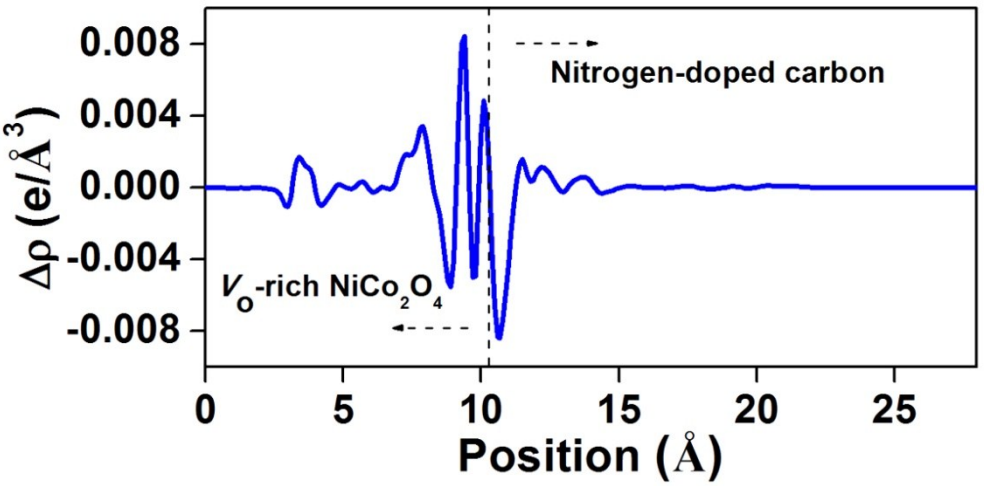

Figure S34. Bader charge analysis of average atoms near the interface of nitrogen-doped carbon and V_o-rich $NiCo_2O_4$.

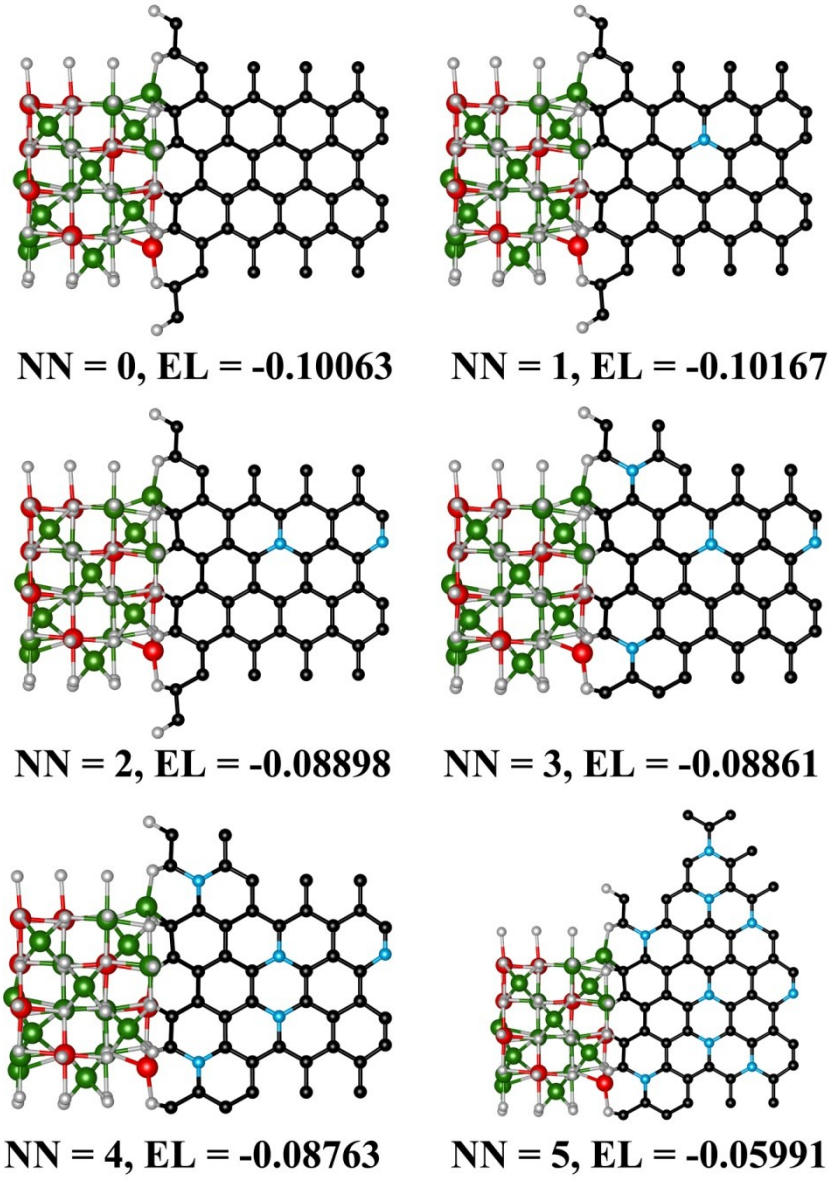

Figure S35. Atomic structures with different nitrogen doping amount. (Here, "NN" and "EL" are the abbreviations of the number of nitrogen atoms in the nitrogen-doped carbon structure and the electron loss per atom.)

From the perspective of theoretical calculation results (Figure S35), the non-doped carbon template shows a more positive EL value than that of nitrogen doped carbon (NN=1), which demonstrates that slightly doped nitrogen is beneficial for the electron transfer from carbon template to the V_o-rich $NiCo_2O_4$ nanosheets. However, this electron transfer is gradually confined by increasing the NN from 1 to 5, which means a relatively low nitrogen amount is beneficial for the electron transfer.

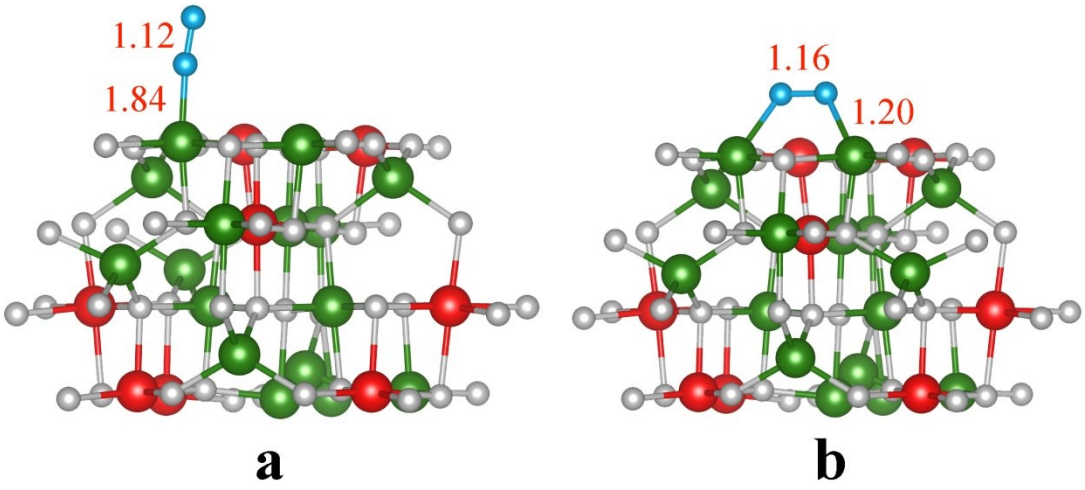

Figure S36. Optimized structures of N_2 adsorption on the surface of a) V_o-poor $NiCo_2O_4$ and b) V_o-rich $NiCo_2O_4$ for end-on and side-on configurations, respectively. The key bond lengths (Å) are also given.

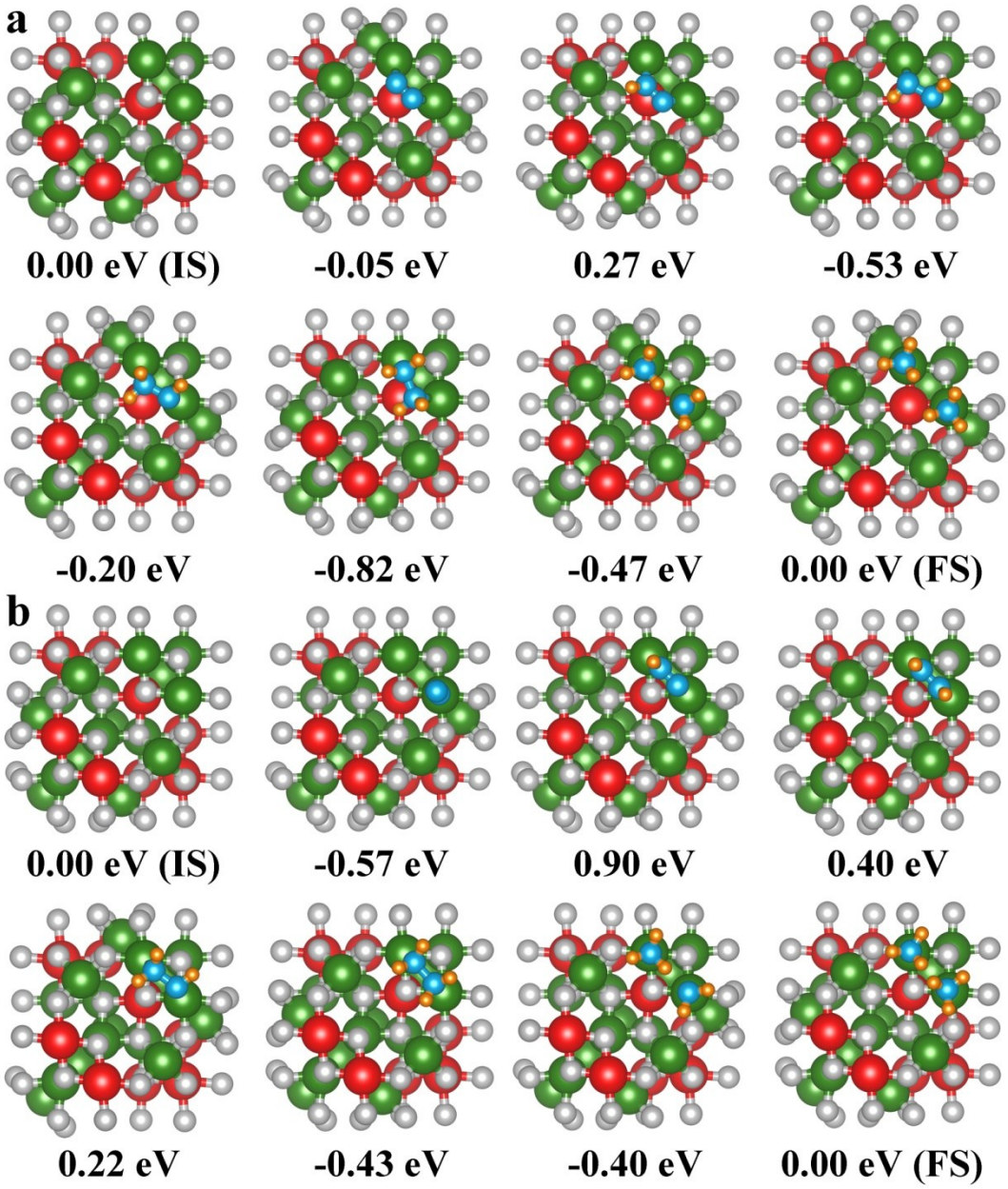

Figure S37. N_2 reduction reaction process on a) V_o-rich $NiCo_2O_4$ and b) V_o-poor $NiCo_2O_4$. IS and FS indicate initial state and final state correspondingly. Red, green, grey, light blue, and orange are nickel, cobalt, oxygen, nitrogen, and hydrogen, respectively.

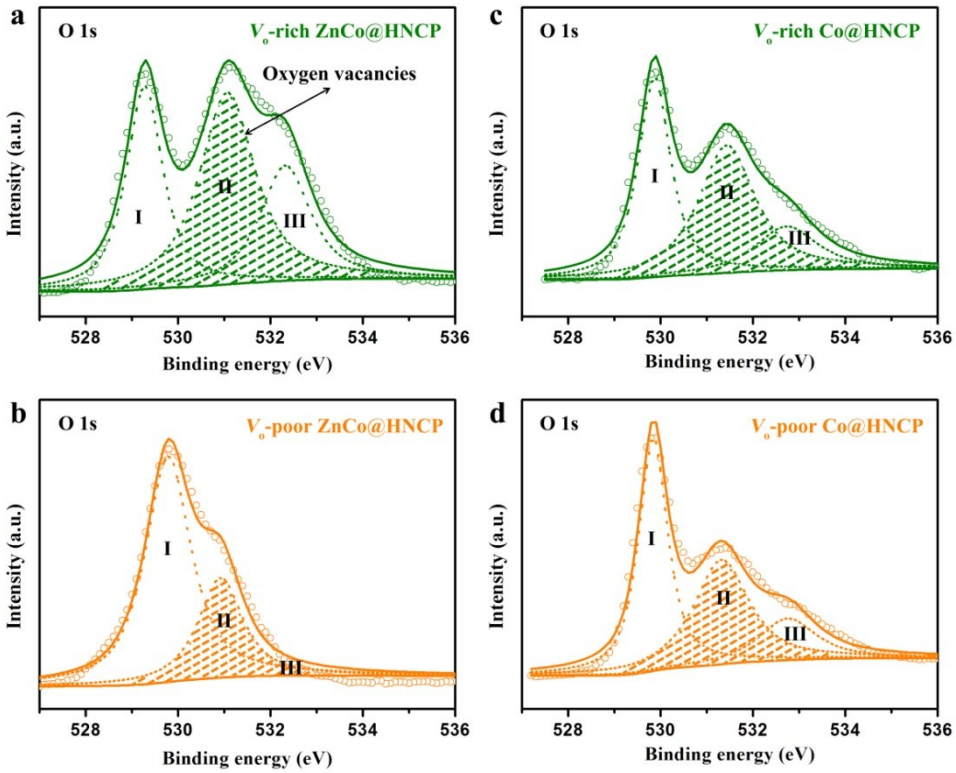

Figure S38. XPS O 1s spectra of a) V_o-rich ZnCo@HNCP, b) V_o-poor ZnCo@HNCP, c) V_o-rich Co@HNCP, and d) V_o-poor ZnCo@HNCP.

The peaks at 529.4, 531.1 and 532.3 eV are associated with lattice oxygen, oxygen vacancies or defects with lower oxygen coordination, and surface adsorbed water molecules, respectively. Obviously, the areas of peak Ⅱ of V_o-rich ZnCo@HNCP and V_o-rich Co@HNCP are much higher than that corresponding V_o-poor ones, indicating that a larger number of oxygen vacancies are present on the surface of V_o-rich ZnCo@HNCP and V_o-rich Co@HNCP.

Table S1. The analysis reports for the compositions of different kinds of gases (provided by WUHAN NEWRADAR SPECIAL GAS CO., LTD.).

Products		**Purity (%)**
High-purity Ar		≥ 99.999
Impurity content (ppm)	N_2	≤ 5
	O_2	≤ 2
	H_2	≤ 1
	CO	-
	CO_2	-
	H_2O	≤ 4
	Total hydrocarbon (THC)	≤ 2
N_2		≥ 99.99
Impurity content (ppmv)	O_2	≤ 3
	H_2	≤ 1
	H_2O	≤ 3
	CO_2	≤ 3
	CO	
	CH_4	
High-purity N_2		≥ 99.999
Impurity content (ppm)	O_2	≤ 3
	H_2	≤ 1
	H_2O	≤ 5
	CO_2	≤ 3
	CO	
	CH_4	

Table S2. Summary of recent reports of catalysts for N_2 conversion to NH_3.

Process	System/Catalyst	Conditions	yield	FE	Reference
Photocatalysis	BiOBr, H_2O (sacrificial agent)	300 W Xenon, $\lambda > 420$ nm	104.2 μmol h^{-1}	----	*J. Am. Chem. Soc.* **2015**, *137*, 6393.
	Diamond, KI (sacrificial agent)	$\lambda > 190$ nm	0.8 ppm (24 h)	----	*Nat. Mater.* **2013**, *12*, 836.
	Graphitic-C_3N_4, methanol, H_2O	$\lambda > 420$ nm	1.24 mmol h^{-1} g^{-1}	----	*J. Mater. Chem. A* **2015**, *3*, 23435.
	FeMoS chalcogels, pyridinium hydrochloride and sodium ascorbate (aq)	150 W Xenon lamp	~0.11 μmol $\mu mol_{catalyst}^{-1}$ h^{-1}	----	*J. Am. Chem. Soc.* **2015**, *137*, 2030.
	BiO quantum dots, H_2O	500 W Xenon lamp	1226 mmol g^{-1} h^{-1}	----	*J. Mater. Chem. A* **2017**, *5*, 201.
	Carbon-$WO_3 \cdot H_2O$, H_2O	500 W Xenon lamp	205 mmol g^{-1} h^{-1}	----	*Chem. Eur. J.* **2016**, *22*, 13819.
	$Ni_2P/Cd_{0.5}Zn_{0.5}S$, H_2O	300 W Xenon lamp, $\lambda > 420$ nm	101.5 μmol h^{-1}	----	*Chem. Eng. J.* **2017**, *307*, 311.
	TiO_2, H_2O (200 mL)	High-pressure Hg lamp, $\lambda > 280$ nm	35 μM (48 h)	----	*J. Am. Chem. Soc.* **2017**, *139*, 10929.
Electrocatalysis	Au-TiO_2 sub-nanocluster, 0.1 M HCl	Room temperature and atmospheric pressure	21.4 μg h^{-1} mg^{-1}	8.11%	*Adv. Mater.* **2017**, *29*, 1606550.
	Au nanorods, 0.1 M KOH	Room temperature and atmospheric pressure	1.648 μg h^{-1} cm^{-2}	3.88%	*Adv. Mater.* **2017**, *29*, 1604799.
	Li^+-incorporation poly(N-ethyl-benzene-1,2,4,5-tetracarboxylic diimide), 0.5 M Li_2SO_4	Room temperature and atmospheric pressure	1.58 μg h^{-1} cm^{-2}	2.85%	*J. Am. Chem. Soc.* **2017**, *139*, 9771.

	Au/CeO-RGO, 0.1 $_M$ HCl	Room temperature and atmospheric pressure	8.3 μg h^{-1} mg^{-1}	10.1%	*Adv. Mater.* **2017**, *29*, 1700001.
	Fe_2O_3/CNT, $KHCO_3$	Room temperature and atmospheric pressure	0.22 μg h^{-1} cm^{-2}	<0.05 %	*Angew. Chem. Int. Ed.* **2017**, *56*, 2699.
	Polypyrrole, 0.1 $_M$ Li_2SO_4, 0,03 $_M$ H^+ solution	60 bar N_2	901 μg (5 h)	----	*J. Electroanal. Chem.* **2010**, *638*, 119.
	ZnSe, 1 $_M$ KOH	Room temperature	391 μg h^{-1} cm^{-2}	1.3%	*J. Electroanal. Chem.* **1990**, *291*, 269.
	Mo nanofilm, 0.01 $_M$ H_2SO_4	Room temperature and atmospheric pressure	1.89 μg h^{-1} cm^{-2}	0.72%	*J. Mater. Chem. A* **2017**, *5*, 18967.
	Pt/C, solid state electrolyte	Room temperature and atmospheric pressure	69.77 μg h^{-1} cm^{-2}	0.55%	*Sci. Rep.* **2013**, *3*, 1145.
	Amorphous $Bi_4V_2O_{11}$-crystalline CeO_2 hybrid, 0.1 $_M$ HCl	Room temperature and atmospheric pressure	23.21 μg h^{-1} mg^{-1}	10.16 %	*Angew. Chem.* **2018**, *130*, 6181.
	Ru/C, solid polymer electrolyte	20 °C	0.21 μg h^{-1} cm^{-2}	0.28%	*Chem. Commun.* **2000**, *17*, 1673.
	V_o-poor $NiCo_2O_4$@HNCP	Room temperature and atmospheric pressure	1.6 μg h^{-1} cm^{-2} or 6.9 μg h^{-1} mg^{-1}	1.8%	This work
	V_o-rich $NiCo_2O_4$@HNCP	Room temperature and atmospheric pressure	4.1 μg h^{-1} cm^{-2} or 17.8 μg h^{-1} mg^{-1}	5.3%	This work
Harsh conditions	Fe/Ru (Haber-Bosch method)	350~550 °C, 200~300 atm	~20% (N_2 conversi	----	*Chem. Soc. Rev.* **2014**, *43*, 5183.

			on rate)		
	Ru (7.8 wt%)-Y_5Si_3	400 °C	32.3 μg h^{-1} mg^{-1}	----	*J. Am. Chem. Soc.* **2016**, *138*, 3970.
	Pd, perovskite-type solid electrolyte $SrCe_{0.95}Yb_{0.05}O_3$	570 °C	275.4 μg h^{-1} cm^{-2}	----	*Science* **1998**, *282*, 98.
	Fe_2O_3, molten hydroxide	250 °C, 25 bar N_2	35% (N_2 conversion rate)	----	*Science* **2014**, *345*, 637.
	$Pr_{0.6}Ba_{0.4}Fe_{0.8}Cu_{0.2}O_{3-\delta}$, mixed electrolyte	400 °C	6.55 μg h^{-1} cm^{-2}	----	*App. Catal. B-Environ.* **2014**, *212*, 152.

FE: Faradaic efficiency.

Table S3. The free energies of various states during NRR process.

States	**Free energy (eV)**	
	V_o-rich $NiCo_2O_4$	**V_o-poor $NiCo_2O_4$**
NN*	-0.05	-0.57
NNH*	0.28	0.89
HNNH*	-0.54	0.40
$HNNH_2$*	-0.20	0.22
H_2NNH_2*	-0.82	-0.42
H_2N*	-0.46	-0.41

5. References:

[1] J. P. Perdew, K. Burke and M. Ernzerhof, *Phys. Rev. Lett.*, 1996, ***77***, 3865.

[2] H. J. Monkhorst and J. D. Pack, *Phys. Rev. B: Solid State*, 1976, ***13***, 5188.

[3] G. Henkelman and H. Jónsson, *J. Chem. Phys.*, 2000, ***113***, 9978.

[4] J. X. Zhao and Z. F. Chen, *J. Am. Chem. Soc.*, 2017, ***139***, 12480.

[5] S. Suarez and D. Paterno, *J. Power Sources*, 2016, ***331***, 544.

[6] S. Z. Andersen, V. Čolić, S. Yang, J. A. Schwalbe, A. C. Nielander, J. M. McEnaney, K. Enemark-Rasmussen, J. G. Baker, A. R. Singh, B. A. Rohr, M. J. Statt, S. J. Blair, S. Mezzavilla, J. Kibsgaard, P. C. K. Vesborg, M. Cargnello, S. F. Bent, T. F. Jaramillo, I. E. L. Stephens, J. K. Nørskov and I. Chorkendorff, *Nature*, 2019, ***570***, 504.

[7] B. H. R. Suryanto, H.-L. Du, D. Wang, J. Chen, A. N. Simonov and D. R. MacFarlane, *Nat. Catal.*, 2019, ***2***, 290.

[8] B. Hu, M. Hu, L. Seefeldt and T. L. Liu, *ACS Energy Lett.*, 2019, ***4***, 1053.

[9] H. Du, T. R. Gengenbach, R. Hodgetts, D. R. MacFarlane and A. N. Simonov, *ACS Sustainable Chem. Eng.*, 2019, ***7***, 6839.

[10] M. A. Shipman and M. D. Symes, *Electrochim. Acta*, 2017, ***258***, 618.

[11] G. W. Watt and J. D. Chrisp, *Anal. Chem.*, 1952, ***24***, 2006.